ARL-TR-10182 ● SEP 2025

Reevaluating the Condensed-Phase Enthalpy-of-Formation of Nitrocellulose from Oligomers to Bulk: Addressing Variability in Prior Studies through Computational Modeling

by Jeffrey D. Veals, Chiung-Chu Chen, Joshua L. Lansford, and Christopher P. Stone

DISTRIBUTION STATEMENT A. Approved for public release: distribution unlimited.

NOTICES

Disclaimers

The findings in this report are not to be construed as an official Department of the Army position unless so designated by other authorized documents.

Citation of manufacturer's or trade names does not constitute an official endorsement or approval of the use thereof.

Destroy this report when it is no longer needed. Do not return it to the originator.

ARL-TR-10182 ● SEP 2025

Reevaluating the Condensed-Phase Enthalpy-of-Formation of Nitrocellulose from Oligomers to Bulk: Addressing Variability in Prior Studies through Computational Modeling

Jeffrey D. Veals, Chiung-Chu Chen, Joshua L. Lansford, and Christopher P. Stone
DEVCOM Army Research Laboratory

DISTRIBUTION STATEMENT A. Approved for public release: distribution unlimited.

REPORT DOCUMENTATION PAGE

1. REPORT DATE	2. REPORT TYPE	3. DATES COVERED	
		START DATE	END DATE
September 2025	Technical Report	1 April 2025	31 July 2025

4. TITLE AND SUBTITLE
Reevaluating the Condensed-Phase Enthalpy-of-Formation of Nitrocellulose from Oligomers to Bulk: Addressing Variability in Prior Studies through Computational Modeling

5a. CONTRACT NUMBER	5b. GRANT NUMBER	5c. PROGRAM ELEMENT NUMBER
5d. PROJECT NUMBER	**5e. TASK NUMBER**	**5f. WORK UNIT NUMBER**

6. AUTHOR(S)
Jeffrey D. Veals, Chiung-Chu Chen, Joshua L. Lansford, and Christopher P. Stone

7. PERFORMING ORGANIZATION NAME(S) AND ADDRESS(ES)	8. PERFORMING ORGANIZATION REPORT NUMBER
DEVCOM Army Research Laboratory ATTN: FCDD-RLA-WC Aberdeen Proving Ground, MD 21005	ARL-TR-10182

9. SPONSORING/MONITORING AGENCY NAME(S) AND ADDRESS(ES)	10. SPONSOR/MONITOR'S ACRONYM(S)	11. SPONSOR/MONITOR'S REPORT NUMBER(S)

12. DISTRIBUTION/AVAILABILITY STATEMENT
DISTRIBUTION STATEMENT A. Approved for public release: distribution unlimited.

13. SUPPLEMENTARY NOTES
ORCIDs: Jeffrey D. Veals, 0000-0002-8238-345X; Joshua L. Lansford, 0000-0001-8245-3190; Chiung-Chu Chen, 0000-0002-8666-9949; Christopher P. Stone, 0000-0002-9621-5334
Minor editorial adjustments to correct syntax/typos were made to abstract and pages 1, 2, 13, 19, and 22.

14. ABSTRACT
This study presents state-of-the-art modeling predictions for the condensed-phase enthalpy-of-formation of neat mono-, di-, and tri-nitrated nitrocellulose (NC) oligomers (*n*) and various oligomer "blends." Deriving estimates for the blends using a previously developed Monte-Carlo weighting approach, we also obtained estimates for various weight-percent nitrogen contents that correspond to several important forms of NC commonly used in propellant formulations. Gas-phase enthalpies of formation were estimated with quantum chemical calculations, employing an isodesmic reaction scheme. Equilibrium molecular dynamics (EMD) simulations were performed with the AMBER force field, incorporating in-house optimized parameters tailored to the nitrate ester functionality. EMD-based density, cohesive energy, solubility parameter, and enthalpy-of-sublimation estimates were obtained. Dependences of these property predictions on the number of monomers per oligomer (*n*), degree of nitration, and temperature were evaluated and found to have merit in comparison with available measured values. Additionally, enthalpies of vaporization were estimated using a previously developed machine learning (ML) model. Condensed phase enthalpy-of-formation estimates were obtained by combining the gas-phase enthalpy-of-formation estimates with enthalpy-of-sublimation and enthalpy-of-vaporization estimates from the EMD simulations and ML model, respectively. Lastly, independent estimates of the condensed-phase enthalpy-of-formation were obtained by using a previously developed quantum mechanics-based program (EDAT). Predictions based on these three approaches were evaluated in context with measured values, and it was found that coupling EMD estimates of the enthalpy-of-sublimation with gas phase enthalpy-of-formation estimates provides a systematic means of obtaining accurate computational estimates of the condensed phase enthalpy-of-formation of NC with respect to nitrogen content.

15. SUBJECT TERMS
Weapons Sciences, propellant, nitrocellulose, quantum chemistry, molecular dynamics, enthalpy-of-formation, machine learning, ML, directed-message passing neural network, D-MPNN

16. SECURITY CLASSIFICATION OF:			17. LIMITATION OF ABSTRACT	18. NUMBER OF PAGES
a. REPORT	b. ABSTRACT	C. THIS PAGE		
UNCLASSIFIED	UNCLASSIFIED	UNCLASSIFIED	UU	44

19a. NAME OF RESPONSIBLE PERSON	19b. PHONE NUMBER *(Include area code)*
Jeffrey D. Veals	(520) 942-1877

STANDARD FORM 298 (REV. 5/2020)
Prescribed by ANSI Std. Z39.18

Contents

List of Figures iv

List of Tables v

Acknowledgments vi

1. Introduction 1

2. Computational Details 2

2.1 Basic Representations of the NC Monomer Unit 2

2.2 EMD Simulation Set and Protocol 2

2.3 Thermodynamic Parameters 7

3. Results and Discussion 7

3.1 Density Estimates 8

3.2 Cohesive Energy, Enthalpy-of-Sublimation, and Solubility Parameter Estimates 12

3.2.1 Cohesive Energy Estimates 12

3.2.2 Enthalpy-of-Sublimation Estimates 14

3.2.3 Solubility Parameter Estimates 16

3.3 Enthalpy-of-Formation Estimates at 298 K 17

4. Summary and Conclusion 23

5. References 25

Appendix. X-OXMN-*n* (X = M, D, T) Oligomer Gas-Phase Enthalpies-of-Formation at 298 K 29

List of Symbols, Abbreviations, and Acronyms 35

Distribution List 36

List of Figures

Figure 1. Stoichiometry, chemical name, SMILES string, and structure of each fundamental monomer unit representation. 2

Figure 2. Stepwise approach used to generate topology, set up the system, and run simulations to obtain property estimates. Shown here for a single system and repeated across all oligomers. 3

Figure 3. Subset of nine model oligomers investigated: mono-, di-, and tri-nitrated species with 1, 2, and 5 monomer units. 4

Figure 4. Representative model of the M-OXMN-2 mononitrate oligomer, consisting of two polymer units each containing one nitrate ester group. This model illustrates the range of AMBER GAFF atom types used in molecular dynamics simulations of the various systems studied (up to nine unique types). 4

Figure 5. Selected frames from NPT simulations: a) M-OXMN-1 and b) T-OXMN-6. 8

Figure 6. Density $\rho(T)$ estimates of NC oligomers as a function of oligomer length and temperature. Panels (a–c) show data for mono-, di-, and tri-nitrated NC oligomers (n = 1–6). Bar graphs display density at 298 K (ρ(298 K)) vs. oligomer length, while scatter plots show $\rho(T)$ for each oligomer length. 10

Figure 7. Cohesive energy ($E_{coh}(T)$) of NC oligomers as a function of oligomer length and temperature. Panels (a–c) show data for mono-, di-, and tri-nitrated NC oligomers (n = 1–6). Bar graphs display cohesive energy at 298 K ($E_{coh}(298\ K)$) vs. oligomer length, while scatter plots show $E_{coh}(T)$ for each oligomer length. 13

Figure 8. Enthalpy-of-sublimation ($\Delta H_{sub}(T)$) of NC oligomers as a function of oligomer length and temperature. Panels (a–c) show data for mono-, di-, and tri-nitrated NC oligomers (n = 1–6). Bar graphs display enthalpy-of-sublimation at 298 K ($\Delta H_{sub}(298\ K)$) vs. oligomer length, while scatter plots show $\Delta Hsub(T)$ for each oligomer length. 14

Figure 9. "Per-monomer" enthalpy-of-sublimation ($\Delta H_{sub}(T)$) of NC oligomers as a function of oligomer length and temperature. Panels (a–c) show data for mono-, di-, and tri-nitrated NC oligomers (n = 1–6). Bar graphs display "per-monomer" enthalpy-of-sublimation at 298 K ($\Delta H_{sub}(298\ K)$) vs. oligomer length, while scatter plots show $\Delta H_{sub}(T)$/monomer for each oligomer length. 15

Figure 10. Comparison of calculated and experimental solubility parameters for NC. Monte-Carlo weighting was used for X-OXMN-n (X = M, D, T), with values based on n = 6 and extrapolated to n = 200. 17

Figure 11. Enthalpy-of-formation $\Delta_f H_s$(298 K) of NC as a function of niotrogen weight percentages and compared with literature data. ... 23

Figure A-1. AMBER-based $\Delta H_{sub}(298\ K)$ values and their best fit to the three-parameter rational model (Type I); units in kcal/mol. 33

List of Tables

Table 1. Atom name, atom type, and partial charges of each atom of the M-OXMN-2. 5

Table 2. Number of atoms and molecules per simulation system. 6

Table 3. AMBER *ρ(T)* estimates for M-OXMN-*n*, D-OXMN-*n*, and T-OXMN-*n* (*n* = 1–6) at 1 atm. 9

Table 4. Monte-Carlo distribution. 11

Table 5. Experimental and simulated reference densities of NC. 12

Table 6. Enthalpy-of-formation estimates for M-OXMN-*n*, D-OXMN-*n*, and T-OXMN-*n* (*n* = 1–10). 18

Table 7. Estimates of the enthalpies-of-formation $\Delta_f H_s(298\ \mathrm{K})$ for mono-, di-, and tri-nitrate NC along with the regression equation used for extrapolation up to oligomer (*n* = 200). 19

Table 8. Enthalpies of formation $\Delta_f H_s(298\ \mathrm{K})$ corresponding to various nitrogen weight percentages. 20

Table 9. Literature data on standard enthalpies of formation $\Delta_f H_s(298\ \mathrm{K})$ at 298 K for NC. 20

Table 10. Enthalpy-of-formation estimates for M-OXMN-*n*, D-OXMN-*n*, and T-OXMN-*n* (*n* = 1–6), which were obtained using various approaches. 22

Table A-1. Estimates of the enthalpy-of-formation $\Delta_f H_g(298\ \mathrm{K})$ and linear regression parameters for low-level models. 31

Table A-2. Molecule structures for target species listed in Table A-1. 32

Table A-3. AMBER-based $\Delta H_{sub}(298\ K)$ and the regression equation for extrapolation up to oligomer (*n*) = 200. 33

Table A-4. DFTBA estimates of the enthalpies-of-formation $\Delta_f H_s(298\ \mathrm{K})$ and the regression equation used for extrapolation up to *n* = 200. 34

Acknowledgments

This research was supported by the U.S. Army Combat Capabilities Development Command (DEVCOM) Army Research Laboratory (ARL) Machine Learning to Accelerate Detailed Finite-Rate Chemical Kinetics Mechanism Creation program. Molecular dynamics simulations and quantum chemistry calculations utilized DoD High Performance Computing Modernization Program resources. We also thank Dr. Edward F. Byrd for giving us permission to run EDAT code.

1. Introduction

Nitrocellulose (NC), derived from the naturally abundant polymer cellulose (Li et al. 2011; Poletto et al. 2014), has been a material of significant scientific, industrial, and military interest for nearly two centuries. Produced by reacting cellulose with strong acids and acid mixtures (Urbanski 1964), NC inherits the semi-crystalline/semi-amorphous structure of its parent material (Svedberg 1947; French 1978; Ioelovich 2024). Its percentage of nitrogen content (typically denoted as x wt% N) varies depending on reaction conditions and cellulose source (Urbanski 1964; Trache et al. 2016). Accurate determination of NC's condensed phase properties, such as the enthalpy-of-formation, is critical for reliable burn rate modeling; yet, discrepancies exist between experimental measurements and values traditionally used in these models (Taylor et al. 1947; Jessup and Prosen 1950). This issue is compounded by the dependence of physicochemical properties on nitration level (Chai et al. 2019, 2020).

The accuracy of these thermochemical values directly impacts the performance predicted by physics-based models used to evaluate energetic material formulations. It has been recognized that different thermochemical codes can use values originating from disparate sources, leading to potentially non-negligible differences in predicted performance. Recent work has sought to address this issue for other common formulation ingredients, such as hydroxyl-terminated polybutadiene (HTPB), by critically assessing literature values and providing clarity on the range of reported enthalpy-of-formation values (Thomas and Petersen 2022). This highlights an ongoing challenge, particularly as new novel energetic materials are synthesized and scaled-up, demanding accurate and reliable thermochemical data.

This technical report presents a novel reassessment of the enthalpy-of-formation of NC at 298 K and 1 atm, employing a combined methodology of molecular dynamics simulations, quantum chemistry calculations, and machine learning (ML) models (an approach proven effective for similar systems) to provide an independent set of estimates. Accurate enthalpy-of-formation values are crucial for physics-based modeling, motivating this investigation. We used our unique modeling framework to assess 18 oligomer systems representing mono-, di-, and tri-nitrated oligomers (n = 1–6) and present results for molecular dynamics-based properties (i.e., density, cohesive energy, solubility parameter, and enthalpy-of-sublimation), ML estimated enthalpy changes, and quantum chemistry-based enthalpy-of-formation. We additionally made extrapolated estimates of these properties for bulk NC with oligomer lengths (n = 200) that fell within the range of experimental molecular weight estimates. These results are discussed herein.

2. Computational Details

The equilibrium molecular dynamics (EMD) protocol used in this study follows the established methodology of our previous work on 1,5,9-decatriene, myrcene (Veals et al. 2023a); hydroxyl-terminated EODT oligomers [HO-(EODT)n-OH] (Veals et al. 2023b); and isopropyl nitrate (Veals et al. 2024). EMD simulations were conducted using the LAMMPS package (Plimpton 1995). Several of our earlier studies largely relied on Class-II force fields—specifically, PCFF (Sun 1995) and COMPASS (Bunte and Sun 2000; McQuaid et al. 2004). However, we have recently leveraged the Class I general AMBER force field (GAFF), as demonstrated in our investigation of isopropyl nitrate. The GAFF parameter set employed here has been previously validated through our studies of nitrate ester plasticizers (Yeh et al. 2017).

2.1 Basic Representations of the NC Monomer Unit

Figure 1 depicts the fundamental monomer units for mono-, di-, and tri-nitrated NC. The scheme also provides the stoichiometry, organic name, and SMILES string for each chemical structure. We have opted to use a shortened naming scheme throughout the report that we derived from the organic name. That is, **M**-OXMN-***n***, **D**-OXMN-***n***, and **T**-OXMN-***n*** (where n = 1–6) represents the **m**ono-, **di**-, and **t**ri-nitrated forms of the oligomer (n) chains up to n = 6.

$C_6H_{11}NO_7$ [(3,4,5-trihydroxy)**ox**an-6-yl]**m**ethyl **n**itrate O=[N+]([O-])OC[CH]1OC[CH](O)[CH](O)[CH]1O	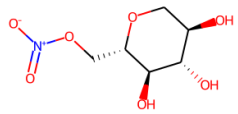
$C_6H_{10}N_2O_9$ [(3-nitrooxy-4,5-dihydroxy)**ox**an-6-yl]**m**ethyl **n**itrate O=[N+]([O-])OC[CH]1OC[CH](O[N+](=O)[O-])[CH](O)[CH]1O	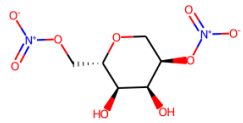
$C_6H_9N_3O_{11}$ [(3,4-dinitrooxy-5-hydroxy)**ox**an-6-yl]**m**ethyl **n**itrate O=[N+]([O-])OC[CH]1OC[CH](O[N+](=O)[O-])[CH](O[N+](=O)[O-])[CH]1O	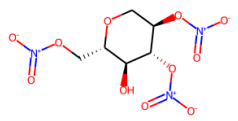

Figure 1. Stoichiometry, chemical name, SMILES string, and structure of each fundamental monomer unit representation.

2.2 EMD Simulation Set and Protocol

The methods and protocols used throughout this study are outlined in Figure 2. Initial topology files for a single oligomer molecule were generated with the

ACPYPE server,* which leverages the Antechamber program within AMBER Tools. Starting from the xyz coordinates of structures optimized using quantum chemistry software (Gaussian 16), the server created the initial structure and assigned atomic charges, which were then manually adjusted (as needed) to achieve a net charge of zero.

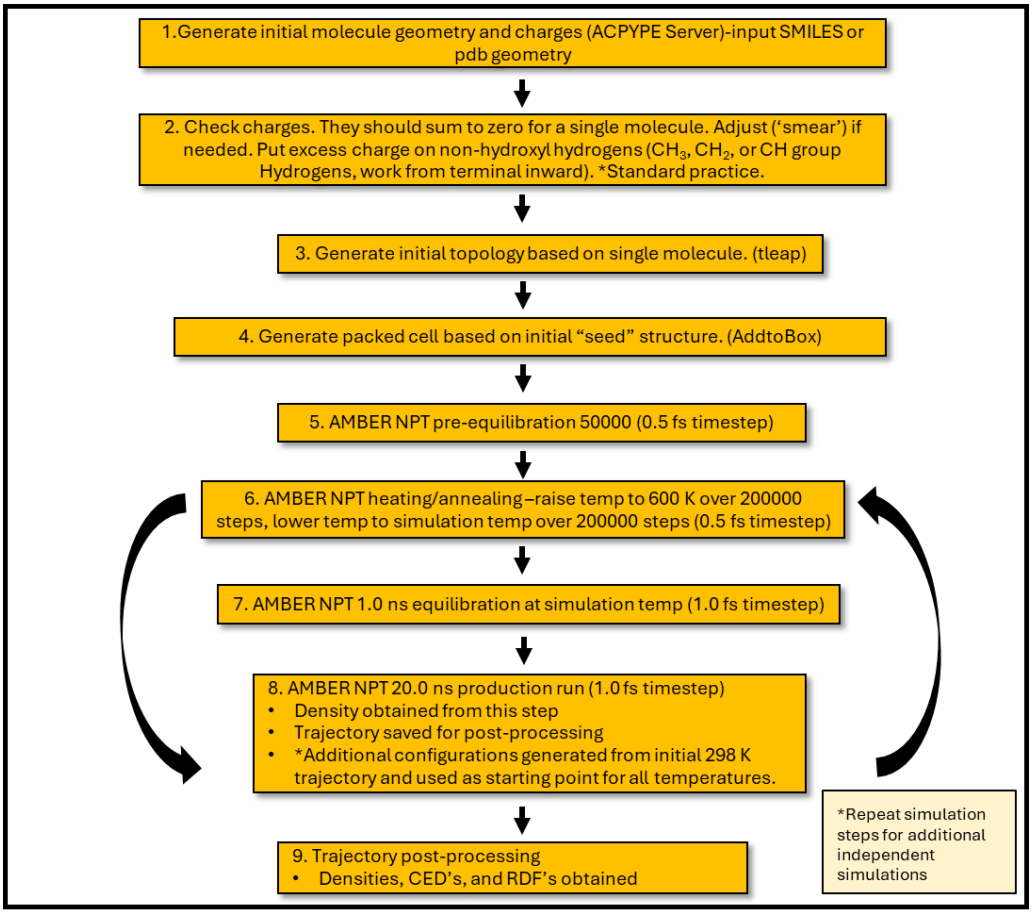

Figure 2. Stepwise approach used to generate topology, set up the system, and run simulations to obtain property estimates. Shown here for a single system and repeated across all oligomers.

Figures 3 and 4 show a subset of the simulated oligomer structures, with Figure 4 specifically highlighting **M**-OXMN-**2** as a representative example. **M**-OXMN-**2** contains all atom types present in the 18 systems, while remaining visually clear. Table 1 details the modified AM1-BCC charges, atom names, and GAFF atom types used for **M**-OXMN-**2**, demonstrating its atom-type assignments as established in our 2017 work with the AMBER force field. We manually created a specific atom type ("ox") because it is not a default in the GAFF force field; this

* https://bio2byte.be/acpype/

allowed us to incorporate nitrate ester-specific parameters from our 2017 work while retaining AMBER defaults for other ether (*"os"*) oxygens.

We then used the AMBER Tools *tleap* program to generate a topology file for a single molecule, adjusting non-bond, bond, and angle parameters for the nitrate ester functionality to match those previously determined (Yeh et al. 2017). AMBER defaults were used for all other parameters. Finally, we created simulation boxes and populated them with molecules using the AMBER Tools *AddToBox* program, maintaining a minimum separation distance of 3.0 angstroms between atoms.

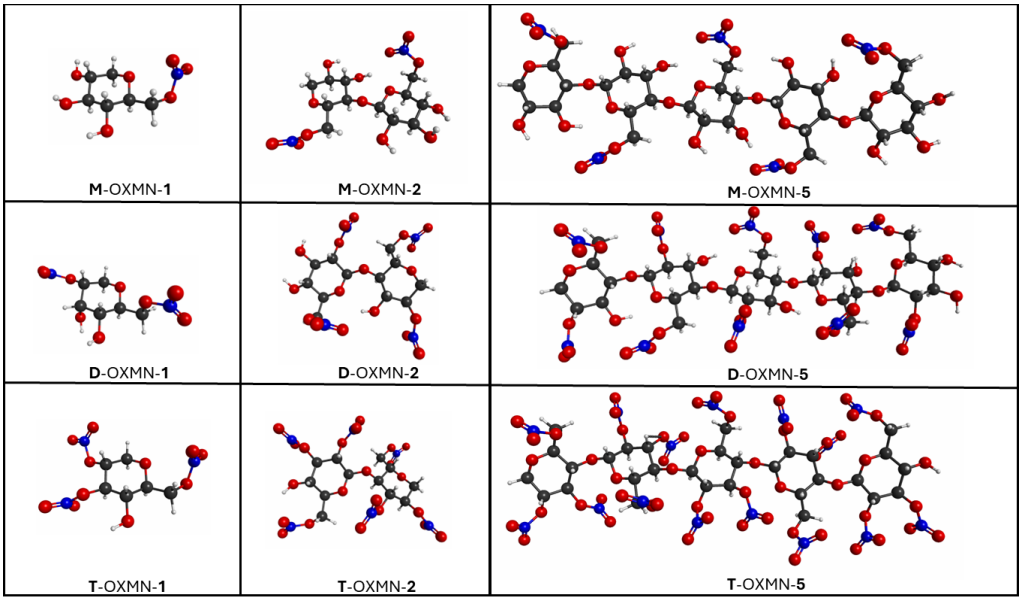

Figure 3. Subset of nine model oligomers investigated: mono-, di-, and tri-nitrated species with 1-, 2-, and 5-monomer units.

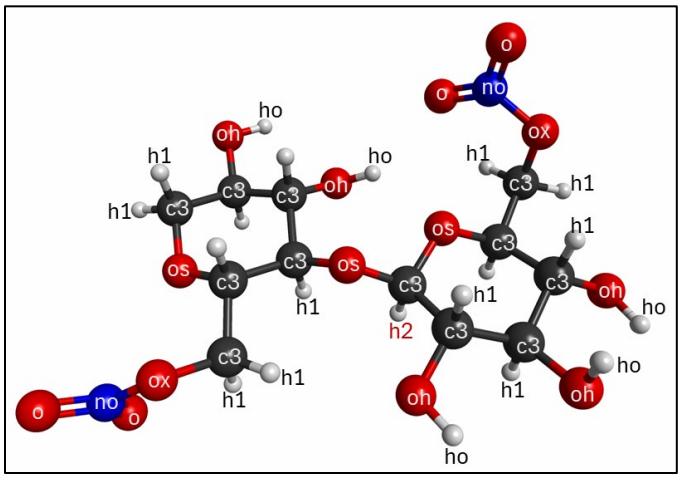

Figure 4. Representative model of the M-OXMN-2 mononitrate oligomer, consisting of two polymer units each containing one nitrate ester group. This model illustrates the range of AMBER GAFF atom types used in molecular dynamics simulations of the various systems studied (up to nine unique types).

Table 1. Atom name, atom type, and partial charges of each atom of the M-OXMN-2.

Atom index	Atom name	Atom type	AM1–BCC partial charges
1	C	c3	0.12740
2	C1	c3	0.11810
3	C2	c3	0.09210
4	C3	c3	0.08810
5	C4	c3	0.10110
6	O	os	–0.40760
7	C5	c3	0.12240
8	O1	ox[a]	–0.34400
9	N	no	0.37920
10	O2	o	–0.17700
11	O3	o	–0.17700
12	H	h1	0.07350
13	O4	oh	–0.59280
14	O5	oh	–0.61180
15	O6	os	–0.39760
16	C6	c3	0.34690
17	C7	c3	0.08710
18	C8	c3	0.06110
19	C9	c3	0.08510
20	C10	c3	0.12610
21	O7	os	–0.44460
22	C11	c3	0.13140
23	O8	ox	–0.34500
24	N1	no	0.38320
25	O9	o	–0.17700
26	O10	o	–0.17700
27	O11	oh	–0.59680
28	O12	oh	–0.59180
29	O13	oh	–0.59480
30	H1	h1	0.07350
31	H2	h1	0.05950
32	H3	h1	0.07150
33	H4	h1	0.07350
34	H5	h1	0.07950
35	H6	h1	0.10900
36	H7	h1	0.10900
37	H8	ho	0.42500
38	H9	ho	0.43700
39	H10	h2	0.06950
40	H11	h1	0.07350
41	H12	h1	0.10650
42	H13	h1	0.06750
43	H14	h1	0.07550
44	H15	h1	0.10900
45	H16	h1	0.10900
46	H17	ho	0.42800
47	H18	ho	0.40900
48	H19	ho	0.42700

[a] The “ox”, atom type is not a default in AMBER. This type was originally defaulted as an ether “os” atom type. We created it to provide the parameters derived in our 2017 report (Yeh et al. 2017) for the non-bond, bond, and angles that involve the nitrate ester ether oxygen. In that report, this was listed as an “os” atom type.

As highlighted in Figure 2, we performed an energy minimization procedure followed by a constant number of particles, pressure, and temperature (NPT) simulation to reduce excessive repulsive interactions between atoms. Based on our previous work demonstrating that properties of interest converge well at approximately 10,000 atoms, we chose not to simulate smaller 5,000-atom systems as done in earlier studies. Therefore, simulations were conducted only using approximately 10,000-atom systems, with the exact number of oligomers per simulation cell dependent on oligomer size. Table 2 provides a detailed listing of systems, total atom counts, and total molecule counts. To maintain a relatively constant atom count, the molecule counts per simulation ranges from 400 to 60, depending on the size of the oligomer.

Table 2. Number of atoms and molecules per simulation system.

Oligomer (*n*)	M-OXMN-n (mononitrate)		D-OXMN-n (dinitrate)		T-OXMN-n (trinitrate)	
	Atoms	**Molecules**	**Atoms**	**Molecules**	**Atoms**	**Molecules**
1	10,000	400	9,720	360	9,860	340
2	9,600	200	9,880	190	10,080	180
3	10,011	141	10,010	130	9,794	118
4	9,400	100	10,200	100	9,900	90
5	9,477	81	10,033	79	9,590	70
6	9,800	70	9,728	64	9,840	60

Atomic coordinates, atom types, and topology information from the pre-equilibrated cells were used to create starting configurations for all temperatures. Each cell underwent a three-stage equilibration process (steps 5–7) before the production runs (step 8), as shown in Figure 2. Electrostatic interactions were calculated using the PPPM implementation of Ewald summation in LAMMPS and van der Waals interactions were modeled with 12-6 Lennard–Jones functions. Constant pressure and temperature were maintained using a Nosé–Hoover barostat and thermostat, respectively.

The equilibration protocol began with a 0.05-ns NPT run at 298 K, followed by a heating/cooling cycle to 600 K over 200,000 steps and back to the target temperature over 200,000 steps (0.5-fs step size), and then a 1.0-ns NPT run at the target temperature, using a 1.0-fs time step. A 20-ns NPT production run was then performed with a 1-fs time step. Thermostat and barostat relaxation times were 0.1 and 1.0 ps, respectively, and coordinates were saved every 10 ps.

To generate diverse trajectories, we re-equilibrated eight frames (spaced approximately 0.5 ns apart) from the initial 298 K production run and launched new simulations at 298, 350, 400, 450, 500, 550, and 600 K, using the same protocol.

The maximum temperature was limited to 600 K, based on results of our previous work. We expect minimal additional insight from higher temperatures.

2.3 Thermodynamic Parameters

To obtain $\Delta_f H_s(T)$ estimates for the oligomer (n) systems, we subtracted EMD-based $\Delta H_{sub}(T)$ estimates from quantum mechanics-electronic structure method (QM-ESM)–based $\Delta_f H_g(T)$ estimates. The $\Delta H_{sub}(T)$ estimates were based on ensemble averages of EMD-generated cohesive energies (E_{coh}), defined as the average intermolecular non-bond energy per mole (Barton 2017), and related to a material's enthalpy-of-sublimation (ΔH_{sub}) by,

$$\Delta H_{sub}(T) \approx E_{coh}\,(T) + RT \tag{1}$$

with R being the universal gas constant.

To accurately compute the gas-phase $\Delta_f H_g(298\,K)$ values for large molecules using quantum chemical methods, we investigated a set of six-membered cyclic compounds and small oligomers (**M**-OXMN-**1**, **D**-OXMN-**1**, and **T**-OXMN-**1**) at both low and high levels of theory. Estimates obtained from lower-level models—including analytic density-functional–based tight-binding (DFTBA) (Zheng et al. 2007), BHandHLYP/3-21G(d) (Becke 1993b), B3LYP/6-31G(2df,p) (Becke 1993a), and M06-2X/6-311+G(2d,2p) (Zhao and Truhlar 2008)—were calibrated against the averaged results obtained from high-level composite methods such as APNO (Ochterski et al. 1996), CBS-QB3 (Montgomery et al. 2000), G4 (Curtiss et al. 2007), G3MP2B3 (Baboul et al. 1999), and several G3MP2-based (Curtiss et al. 1999) approaches (e.g., G3MP2//MPWB95/6-31+G(d,p), G3MP2//B3LYP/6-31G(2df,p), G3MP2//M06-2X/6-31G(2df,p), and G3MP2//M06-2X/6-311+G(2d,2p)). All quantum chemical calculations were performed using Gaussian 16 (Frisch et al. 2016). The isodesmic reaction scheme used and the linear regression parameters for the low-level models are provided in the Appendix, Table A-1; the structures of the six-membered cyclic compounds are listed in Table A-2.

3. Results and Discussion

Figure 5 presents equilibrated NPT simulation cells for **M**-OXMN-**1** and **T**-OXMN-**6** systems, illustrating their representative configurations. Having shorter chains and higher OH content (and thus greater potential for intermolecular hydrogen bonding), resulting in larger per-monomer cohesive energy estimates. As will be discussed, trends in the interaction energy estimates derived from the simulations for **X**-OXMN-***n*** (where X = M, D, or T; n = 1–6) systems are consistent with that observation.

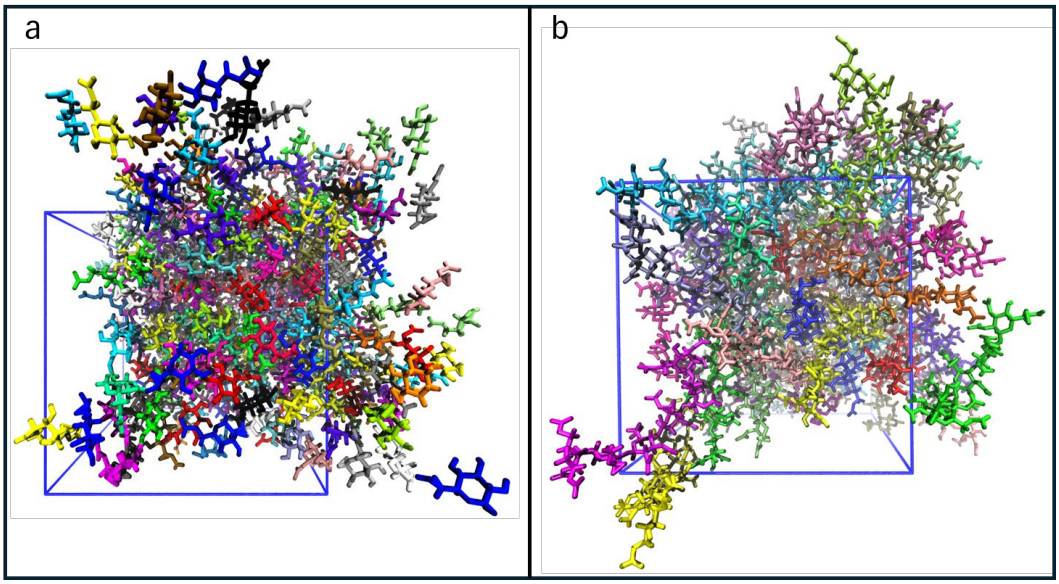

Figure 5. Selected frames from NPT simulations: a) M-OXMN-1 and b) T-OXMN-6.

3.1 Density Estimates

Table 3 presents density, $\rho(T)$, estimates for the various polymeric oligomers (n = 1–6) for each nitration level (**M**ono-, **D**i-, or **T**rinitrate) in the 298–600 K range. Figure 6 presents the data graphically. It was previously found for other nitrate ester systems (Yeh et al. 2017) that AMBER-based estimates are quite reasonable relative to experimental values for the plasticizer molecules studied. In the present case, we expected reasonable values based on our previously optimized AMBER parameters for the nitrate ester groups.

Table 3. AMBER $\rho(T)$[a] estimates for M-OXMN-*n*, D-OXMN-*n*, and T-OXMN-*n* (*n* = 1–6) at 1 atm.

Oligomer (*n*)	298 K	350 K	400 K	450 K	500 K	550 K	600 K
			M-OMXN-***n***				
1	1.49	1.47	1.44	1.40	1.35	1.31	1.26
2	1.51	1.50	1.48	1.46	1.42	1.39	1.35
3	1.51	1.51	1.49	1.48	1.45	1.42	1.38
4	1.52	1.51	1.50	1.49	1.46	1.44	1.40
5	1.52	1.52	1.50	1.49	1.47	1.45	1.41
6	1.51	1.51	1.50	1.49	1.47	1.45	1.42
			D-OMXN-***n***				
1	1.55	1.53	1.50	1.46	1.41	1.36	1.32
2	1.58	1.57	1.55	1.53	1.49	1.45	1.41
3	1.59	1.58	1.56	1.55	1.52	1.48	1.44
4	1.59	1.58	1.57	1.55	1.53	1.49	1.46
5	1.59	1.58	1.57	1.55	1.53	1.50	1.47
6	1.59	1.58	1.57	1.56	1.54	1.51	1.47
			T-OMXN-***n***				
1	1.61	1.59	1.55	1.51	1.46	1.41	1.36
2	1.65	1.63	1.61	1.58	1.53	1.49	1.44
3	1.65	1.64	1.62	1.60	1.56	1.51	1.47
4	1.65	1.64	1.63	1.61	1.57	1.53	1.48
5	1.66	1.64	1.63	1.61	1.58	1.54	1.49
6	1.64	1.64	1.62	1.61	1.59	1.54	1.50

[a] Units in g/cm^3

We had two main questions when monitoring the density values:

1) Primarily, how is density converging with polymer oligomer length?
2) How well does this force-field parameterization predict density values relative to available experimental data?

Addressing the first question, Figure 6 presents bar graphs of the data for a given nitration level (**M** = mono-, **D** = di-, **T** = tri-nitrate ester) at 298 K as functions of oligomer length. We see that for the mono-nitrated "**M**-OXMN-***n***" series the density varies from 1.49 to 1.52. Similarly, for the di-nitrated and tri-nitrated series ("**D**-OXMN-***n***" and "**T**-OXMN-***n***") the density prediction varies from 1.55–1.59 and 1.61–1.66 g/cm^3, respectively. For each oligomer type, the densities began converging to consistent values once an oligomer length of $n = 4$ is reached. The density change is negligeable beyond this length. For the longest length $n = 6$ for the case of **M**-OXMN-**6** and **T**-OXMN-**6**, the density is marginally less than for the $n = 5$ oligomers (**M**-OXMN-**5** and **T**-OXMN-**5**) at 298 K. This is likely caused by the large system getting trapped in "less dense" configurations during the annealing process. This can be seen more clearly by examining the density convergence behavior at higher temperatures. At all temperatures above 298 K, the densities

converge smoothly to have the maximum values correlated to the longest chains; it is only for the 298 K case that the maximum length did not correspond to the maximum converged value.

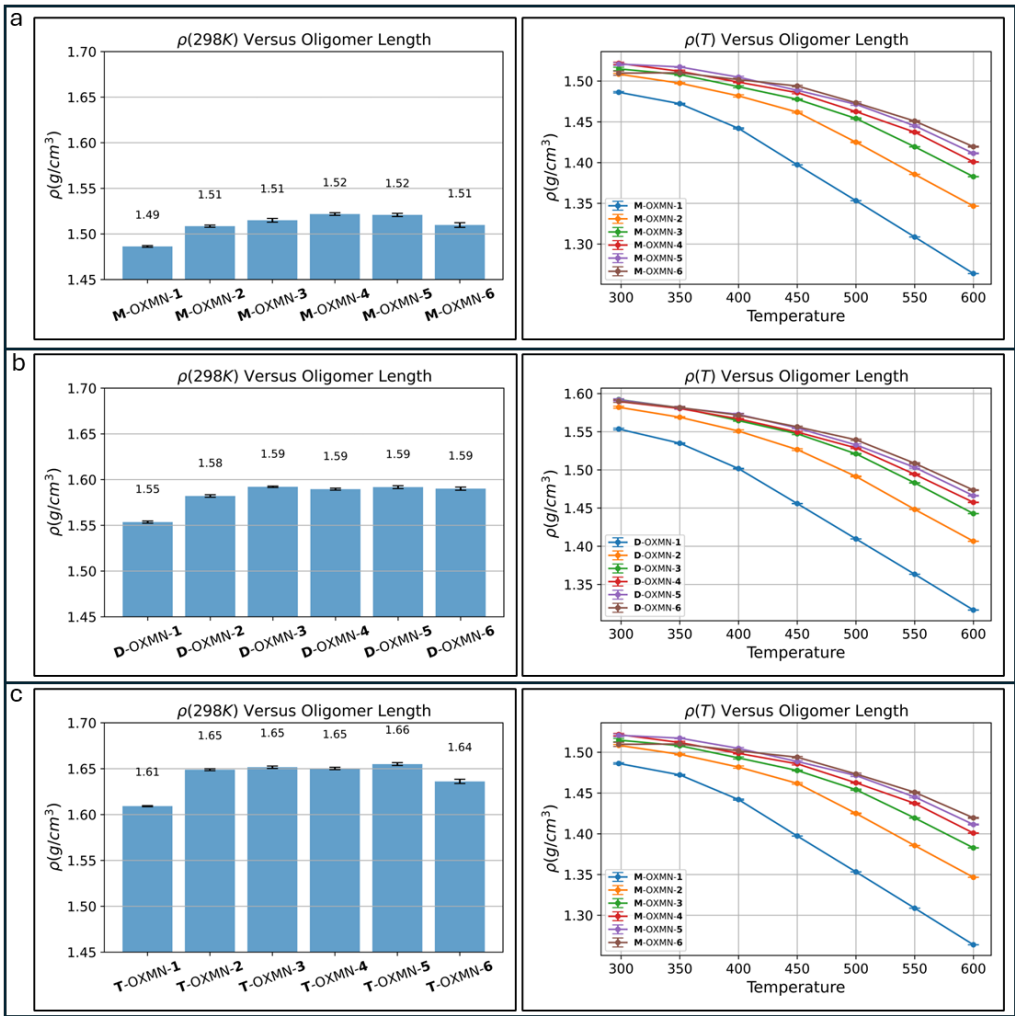

Figure 6. Density $\rho(T)$ estimates of NC oligomers as a function of oligomer length and temperature. Panels (a–c) show data for mono-, di-, and tri-nitrated NC oligomers (n = 1–6). Bar graphs display density at 298 K (ρ(298 K)) vs. oligomer length, while scatter plots show $\rho(T)$ for each oligomer length.

Understanding how the density varies as a function of temperature is also of interest. Trends as a function of temperature are shown to be consistent across each oligomer (n = 1–6) and nitration level (mono-, di-, and tri-). The shorter oligomers have the lowest density at a given temperature, and they have the greatest density decrease over the temperature range considered. As oligomer length increases, the trend as a function of temperature converges similarly to that of the longest oligomers (**X**-OXMN-**6; x = M,D,T**), with the predictions for (**X**-OXMN-***n***; ***n*** = 4–6) having nearly overlapping curves for most of the temperature range.

The second question of how well the force field predicts density values for each nitration level relative to experiment was also considered. Experimentally, only data for percentage nitration levels are known. That is, none of these materials are truly 100% mono-, di-, or tri-nitrated. Thus, comparisons were made to the range of previously available data. To make comparisons more "apples-to-apples" we leveraged the Monte-Carlo–based weightings found in Table 4 (see Miller and Anderson [2003]). Combining those weightings with the density estimates from simulations of pure mono-, di-, and tri-nitrated oligomers (n = 5 or 6) we were able estimate densities associated with nitrogen contents ranging from 10.0% to 14.14% with the assumption that we could simply additively combine the weighted densities obtained from the independent simulations.

Table 4. Monte-Carlo distribution of nitrate mass fractions (Miller and Anderson 2003).

Nitrogen content (%)	Mono-nitrate	Di-nitrate	Tri-nitrate
0.10	0.407[a]	0.375[a]	0.218[a]
0.11	0.275	0.368	0.357
0.126	0.105	0.253	0.642
0.1315	0.060	0.182	0.758
0.135	0.035	0.128	0.838

[a] Mass fraction of each monomer to produce NC at the specified nitrogen %.

Experimental, modeled, and simulated density predictions are dependent on NC source, nitration level, and model type (Gibbon 2024). Therefore, we opted to see if current results fell within previously reported values. Gibbon has compiled NC density values from multiple sources (some of which we have listed here; see Table 5). Reported values range from 1.6 to 1.68 g/cm^3 depending on organic source (wood pulp, cotton linters, etc.), reported temperature, nitration level, structure type, and percent of nitrogen content. The values reported here for our longest oligomers **M**-OXMN-***n***, **D**-OXMN-***n***, and **T**-OXMN-***n*** (n = 5 and 6) range from 1.52 to 1.66 g/cm^3 (see Table 5). As stated above, we additionally performed a Monte-Carlo distribution of the densities, weighting the mono-, di-, and tri-nitrated forms of the longest oligomers.

Table 5. Experimental and simulated reference densities of NC.

Nitrogen content (%)	Density	Reference
. . .	1.6[a]	Richards et al. 2018
14.14	1.619[b]	Richards et al. 2018
6.4–13.41	1.656–1.680[a]	He et al. 2017
11.5–13.15	1.64–1.66[a,c]	French 1978
12.6	1.6–1.64[a,d]	French 1978
9.0–14.00	1.65–1.66[e]	CHEETAH (Fried and Souers 1994)
10.0–14.14	1.58–1.66	Current study[f]

[a] Experimental value. [b] Simulated value of fully nitrated NC. [c] Dry fibrous NC estimates. [d] Milled cotton fiber-based NC powder with particle density varying from 1.6 to 1.64 g/cm^3. [e] These are the defaults used in the thermochemical software (CHEETAH v. 10.1). [f] Values obtained from Monte-Carlo weighting of the densities values of the mono-, di-, and tri-nitrated oligomers (**X**-OXMN-***n*****; X = M,D,T; *n* = 5 or 6**).

In this work, NC with nitrogen wt% levels ranging from 10.0 to 14.14 had simulated densities of 1.58 to 1.66 g/cm^3 (see Table 5). This aligns with the results reported by Gibbon (2024) and other sources. The trend is consistent with the higher nitration levels corresponding to the higher densities. It is worth mentioning that our results represent purely amorphous NC forms (i.e., no semi-crystallinity). French (1978) suggested a value of 1.6 for amorphous NC with 12.6% nitrogen content (based on experimental results of milled NC). The tri-nitrated systems correspond closest to 14.14% nitrogen content (i.e., a theoretical maximum). Measured values for NC 13.3% and 13.41% N are 1.67 and 1.68 g/cm^3 (He et al. 2017). Additionally, a computed value based on a custom force field (with combined parameters from a GAFF and OPLS force field) predicted a value of 1.619 g/cm^3 based on a model representation of the fully tri-nitrated NC dimer with a crystalline orthorhombic unit cell (Richards et al. 2018). Overall, comparisons to NC density values reported in literature suggest our model produces reasonable density predictions.

3.2 Cohesive Energy, Enthalpy-of-Sublimation, and Solubility Parameter Estimates

3.2.1 Cohesive Energy Estimates

We can calculate the cohesive energy (E_{coh}) of each system from EMD results. As implemented in LAMMPS, this is the total non-bond "intermolecular" interaction energy (i.e., excludes intramolecular non-bond energy). This represents the energy required to dissociate all intermolecular contacts per mole of condensed material (Barton 2017).

Trends of $E_{coh}(298\ K)$ as a function of oligomer length are shown in Figure 7. We see that for each respective nitration level (mono-, di-, and tri-), E_{coh} increases

smoothly as oligomer length increases. Unlike density, E_{coh} values do not plateau but rather increase logarithmically. More energy is required to break all intermolecular contacts per mole of the longer and bulkier polymer chains. From charts at 298 K, we also see for a given oligomer length (n), as additional nitrate ester groups are added, the cohesive energy increases. This trend is consistently observed for oligomers (n = 2–6). Overall, E_{coh} ranged from approximately 28 (n = 1) to approximately 117 kcal/mol (n = 6).

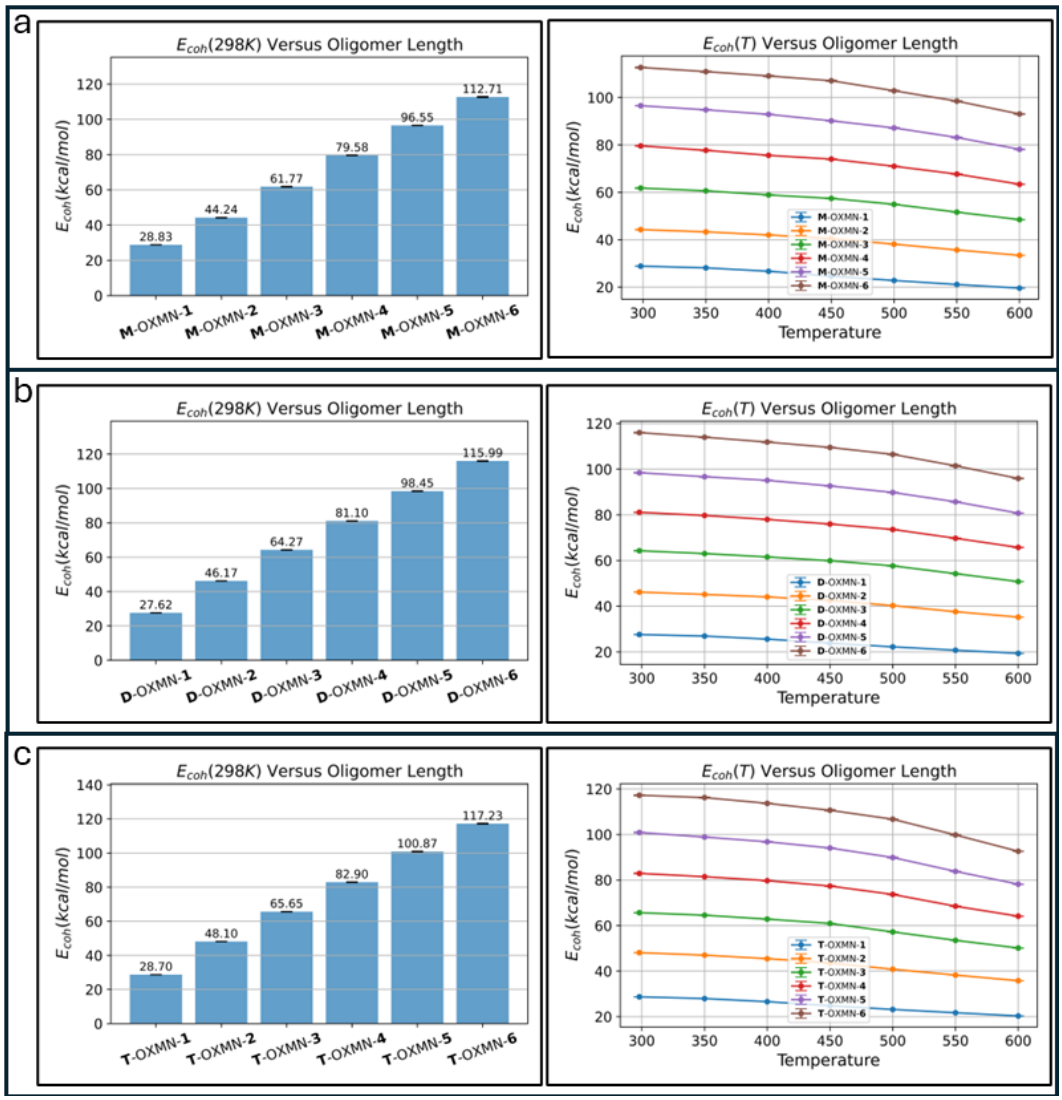

Figure 7. Cohesive energy ($E_{coh}(T)$) of NC oligomers as a function of oligomer length and temperature. Panels (a–c) show data for mono-, di-, and tri-nitrated NC oligomers (n = 1–6). Bar graphs display cohesive energy at 298 K ($E_{coh}(298\ K)$) vs. oligomer length, while scatter plots show $E_{coh}(T)$ for each oligomer length.

3.2.2 Enthalpy-of-Sublimation Estimates

Figure 8 presents the $\Delta H_{sub}(T)$ results, and their dependence on oligomer length at 298 K and temperature. The $\Delta H_{sub}(T)$ decreases with increasing temperature at all oligomer lengths and nitration levels. The decrease in $\Delta H_{sub}(T)$ with temperature is greater for longer oligomer lengths. For the monomers (n = 1), the decrease is 7.7–8.7 kcal/mol depending on nitration level. For the longest oligomers (n = 6), the decrease ranges from 19.1 to 24.0 kcal/mol, where the decrease is largest for the tri-nitrated **T**-OXMN-**6** chains.

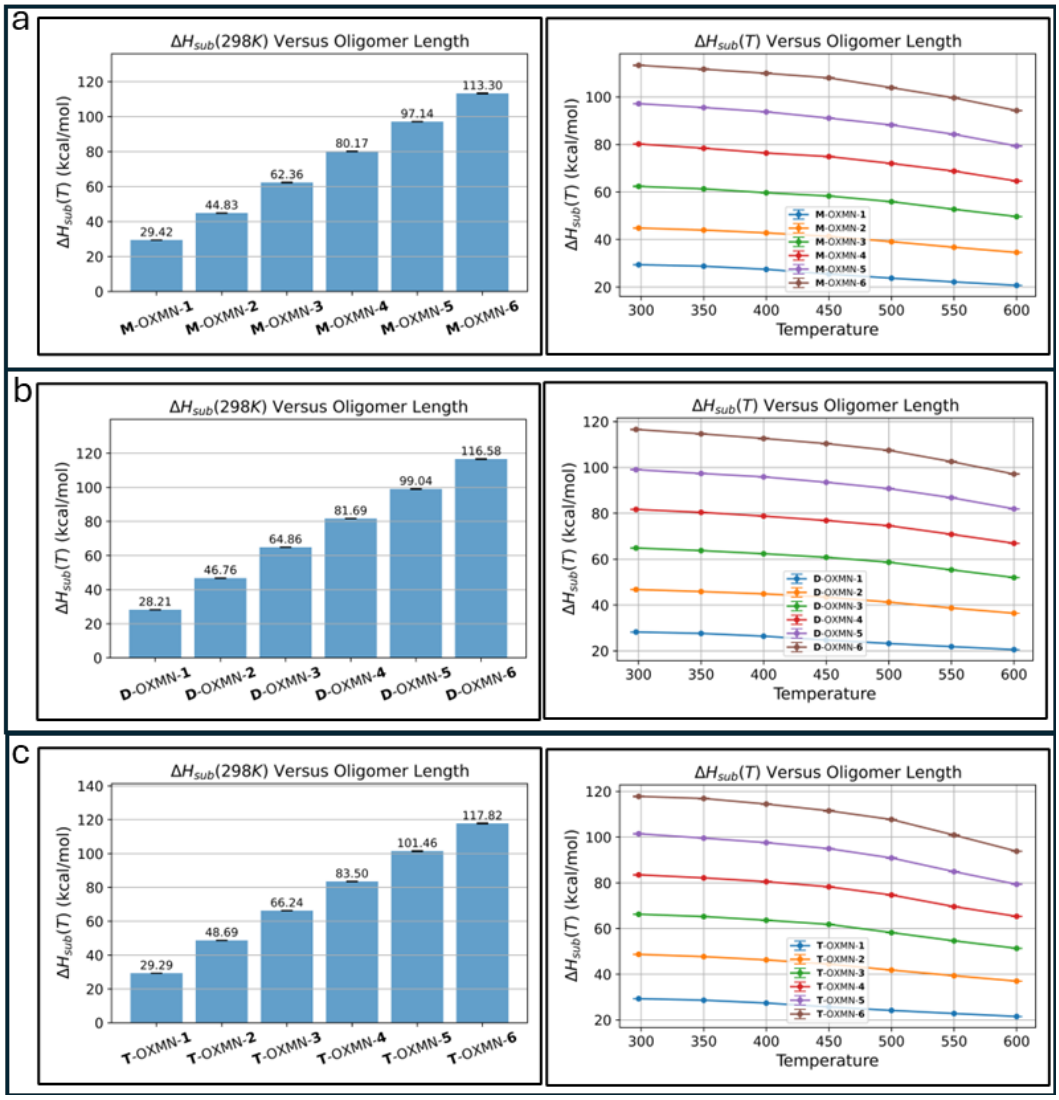

Figure 8. Enthalpy-of-sublimation ($\Delta H_{sub}(T)$) of NC oligomers as a function of oligomer length and temperature. Panels (a–c) show data for mono-, di-, and tri-nitrated NC oligomers (n = 1–6). Bar graphs display enthalpy-of-sublimation at 298 K ($\Delta H_{sub}(298\ K)$) vs. oligomer length, while scatter plots show $\Delta H_{sub}(T)$ for each oligomer length.

We assess $\Delta H_{sub}(T)$ values on a "per-monomer" basis for completeness. Additionally, per-monomer values—as with density—provide a better idea of how $\Delta H_{sub}(T)$ converges toward the "bulk limit." It is another indicator that our longest chains are sufficient in length to capture the amorphous "cohesive" interaction behavior of NC. It is clear from the bar graphs in Figure 9 that the energy is converging smoothly to a per-monomer limit.

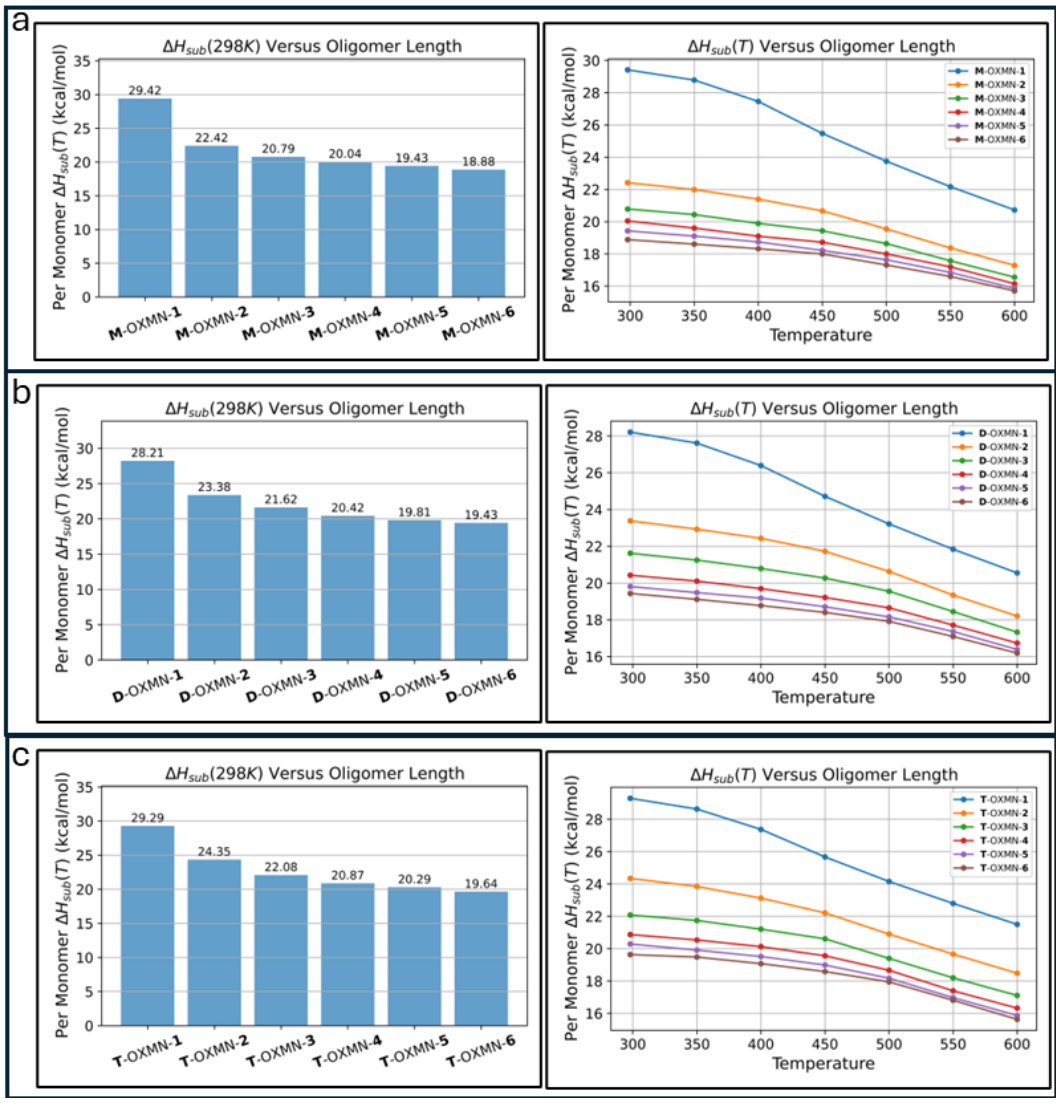

Figure 9. "Per-monomer" enthalpy-of-sublimation ($\Delta H_{sub}(T)$) of NC oligomers as a function of oligomer length and temperature. Panels (a–c) show data for mono-, di-, and tri-nitrated NC oligomers (n = 1–6). Bar graphs display "per-monomer" enthalpy-of-sublimation at 298 K ($\Delta H_{sub}(298\ K)$) vs. oligomer length, while scatter plots show $\Delta H_{sub}(T)$/monomer for each oligomer length.

For the mono-, di-, and tri-nitrated systems the per-monomer heat-of-sublimation value ranges are 29.4–18.9, 28.2–19.4, and 29.3–19.6 kcal/mol, respectively. In these cases, the larger values of each range are for the monomers (**X**-OXMN-**1**,

where **X** = M, D, or T), and smaller values are for the hexamers (**X**-OXMN-**6**, where **X** = M, D, or T) of each respective nitration level. Again, looking at the trends in the behavior as a function of temperature, the magnitudes and the rates of change of each successively longer oligomer system approaches the behavior of the hexamer (n = 6) for each respective nitration level.

3.2.3 Solubility Parameter Estimates

Due to limited experimental and computational data for NC cohesive energy or sublimation enthalpy predictions, we evaluated the reasonableness of our calculated cohesive energies by comparing solubility parameters, for which previous experimental and modeling data is available. Since both enthalpy-of-sublimation and solubility parameters can be derived from cohesive energy in molecular dynamics (MD) simulations, this serves as an indirect validation of our results.

The solubility parameter (δ) is estimated using Equations 2 and 3,

$$\delta = \sqrt{CED}, \tag{2}$$

$$CED = \frac{E_{coh}}{\bar{V}}, \tag{3}$$

where δ is the solubility parameter, *CED* is the cohesive energy density, and $\bar{V}$ is the molar volume (Hildebrand and Scott 1950).

We computed solubility parameters for **M**-OXMN-***n***, **D**-OXMN-***n***, and **T**-OXMN-***n*** oligomers (n = 1–6), corresponding to nitrogen contents of roughly 6.75 wt%, 11.11 wt%, and 14.14 wt% nitrogen, respectively. Like densities, estimates for NC with 10.0%–14.14% nitrogen content were obtained using weighted averages of the **M**-, **D**-, and **T**-OXMN-**6** results (see weightings in Table 4). We also extrapolated each series to the bulk (**M**-OXMN-***n***, **D**-OXMN-***n***, and **T**-OXMN-***n***; ***n*** = 200) and calculated solubility parameters from the extrapolated values (see example in the Appendix, Table A-3).

Experimental data from Kotter and Groven (2022) for NC with 12.2% and 13.4% nitrogen content—along with COMPASS force-field–based MD results from Yang et al. (2014), Meng et al. (2024), and Qi et al. (2019)—provided benchmarks. As shown in Figure 10, our predictions from both six-unit oligomers and bulk extrapolations agree well with these references. Extrapolating to the bulk lowers the value by roughly 1 solubility parameter unit, $(cal \cdot cm^{-3})^{0.5}$, at a given nitration level. The solubility parameter decreases slightly with increasing nitration (from approximately 10.5 to 9.5 $(cal \cdot cm^{-3})^{0.5}$ over the nitration range 10.0%–14.14% nitrogen content), consistent with literature trends. Agreement with available experimental values supports the accuracy of our cohesive energy predictions, providing increased merit for our enthalpy-of-sublimation estimates.

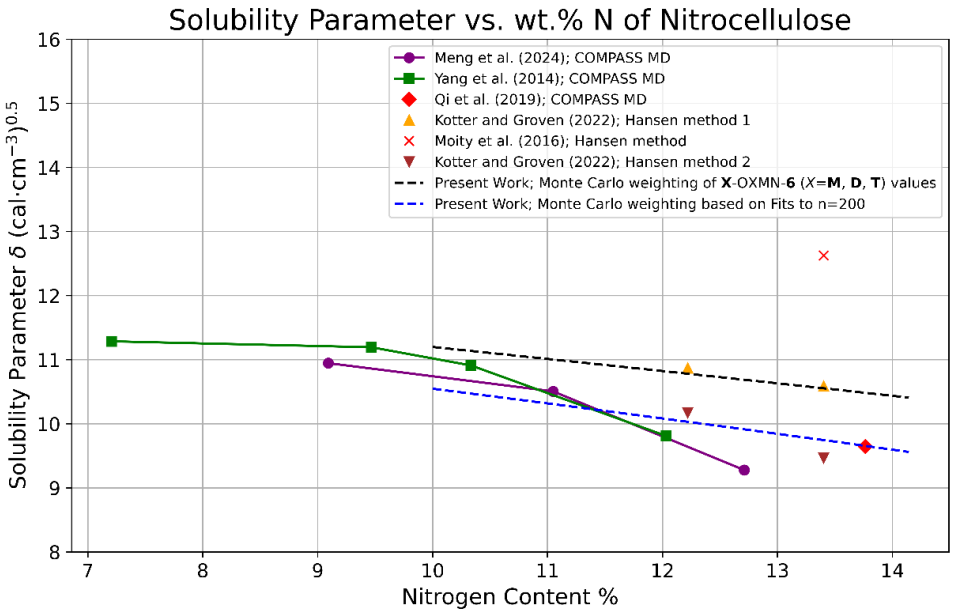

Figure 10. Comparison of calculated and experimental solubility parameters for NC. Monte-Carlo weighting was used for X-OXMN-*n* (X = M, D, T), with values based on *n* = 6 and extrapolated to *n* = 200.

3.3 Enthalpy-of-Formation Estimates at 298 K

Table 6 presents $\Delta_f H_g(298\,K)$ estimates for **M**-OXMN-***n***, **D**-OXMN-***n***, and **T**-OXMN-***n*** (n = 1–10). For oligomers larger than n = 6, only the DFTBA method was applicable due to computational limitations. Based on accuracy considerations, we regard the M06-2X/6-311+G(2d,2p) level of theory (hereafter, M062XBas3-based for brevity) as the most reliable. Therefore, $\Delta_f H_g(298\,K)$ values at this level were extrapolated from the DFTBA results via linear regression. The AMBER-based $\Delta H_{sub}(298\,K)$ estimates for **X**-OXMN-***n*** (X = M, D, T; n = 1–6) were described in Section 3.2 and are also listed in Table 6. For oligomers with n > 6, $\Delta H_{sub}(298\,K)$ values were derived using the three-parameter rational regression model described in the Appendix, Table A-3. The $\Delta_f H_s(298\,K)$ values were obtained by subtracting the AMBER-based ΔH_{sub} estimates from the M062XBas3-based $\Delta_f H_g$ estimates.

Table 6. Enthalpy-of-formation estimates for M-OXMN-*n*, D-OXMN-*n*, and T-OXMN-*n* (*n* = 1–10).

Oligomer	$\Delta_f H_g(298K)$				$\Delta H_{sub}(298\ K)$	$\Delta_f H_s(298\ K)$	
(*n*)	DFTBA[a]	BHBas1[b]	B3LPYBas2[c]	M062XBas3[d]	AMBER-based	DFTBA	M062XBas3
			M-OMXN-***n***				
1	–193.6[e] (–193.6)[f]	–192.4 (–191.2)	–192.8 (–192.1)	–193.7 (–193.1)	29.4	–223.1	–223.2
2	–378.8 (–377.6)	–381.9 (–378.8)	–382.0 (–379.6)	–379.8 (–378.7)	44.8	–423.7	–424.6
3	–566.7 (–564.2)	–571.2 (–566.1)	–570.0 (–566.0)	–568.0 (–566.6)	62.4	–629.0	–630.4
4	–753.2 (–749.6)	–759.0 (–752.0)	–757.8 (–752.1)	–755.2 (–753.5)	80.2	–833.4	–835.4
5	–933.1 (–928.3)	–941.4 (–932.6)	–940.6 (–933.3)	–937.8 (–935.6)	97.1	–1030.2	–1034.9
6	–1123.4 (–1117.4)	–1129.9 (–1119.1)	–1130.0 (–1121.0)	*–1130.2*[g]	113.3	–1236.7	–1243.5
7	–1298.9 (–1291.8)	. . .	. . .	*–1307.1*	*132.0*[h]	–1430.9	–1439.1
8	–1482.5 (–1474.2)	. . .	. . .	*–1492.1*	*149.5*	–1632.1	–1641.7
9	–1437.3 (–1429.3)	. . .	. . .	*–1446.5*	*167.1*	–1604.4	–1613.6
10	–1846.0 (–1835.4)	. . .	. . .	*–1858.4*	*184.7*	–2030.7	–2043.0
			D-OMXN-***n***				
1	–170.8 (–170.9)	–168.5 (–167.5)	–169.7 (–169.2)	–168.9 (–168.3)	28.2	–199.0	–197.1
2	–331.2 (–330.3)	–334.4 (–331.7)	–333.5 (–331.6)	–334.1 (–333.2)	46.8	–378.0	–380.9
3	–492.1 (–490.1)	–497.1 (–492.8)	–494.7 (–491.4)	–498.0 (–496.7)	64.9	–557.0	–562.8
4	–649.0 (–646.0)	–653.1 (–647.2)	–651.6 (–646.9)	–653.5 (–651.9)	81.7	–730.7	–735.2
5	–806.6 (–802.6)	–816.4 (–808.8)	–812.5 (–806.4)	*–811.0*	99.0	–905.6	–910.1
6	–969.7 (–964.7)	–979.7 (–970.5)	–977.0 (–969.5)	*–975.4*	116.6	–1086.3	–1091.9
7	–1121.8 (–1115.8)	. . .	. . .	*–1128.6*	*133.6*	–1255.4	–1262.2
8	–1279.3 (–1272.3)	. . .	. . .	*–1287.4*	*150.7*	–1430.0	–1438.1
9	–1437.3 (–1429.3)	. . .	. . .	*–1446.5*	*167.8*	–1605.1	–1614.3
10	–1590.5 (–1581.5)	. . .	. . .	*–1600.9*	*184.9*	–1775.4	–1785.8
			T-OMXN-***n***				
1	–147.5 (–147.7)	–143.5 (–142.7)	–146.3 (–146.0)	–144.9 (–144.4)	29.3	–176.8	–174.2
2	–283.4 (–282.8)	–283.3 (–281.1)	–282.6 (–281.1)	–284.0 (–283.2)	48.7	–332.1	–332.7
3	–414.1 (–412.7)	–415.4 (–411.9)	–411.3 (–408.7)	–415.4 (–414.3)	66.2	–480.3	–481.6
4	–556.3 (–554.0)	–552.5 (–547.6)	–550.4 (–546.5)	*–558.9*	83.5	–639.8	–642.4
5	–684.8 (–681.6)	–679.3 (–673.1)	–678.3 (–673.3)	*–688.3*	101.5	–786.3	–789.8
6	–815.6 (–811.5)	–808.0 (–800.4)	–807.4 (–801.3)	*–820.1*	117.8	–933.4	–937.9
7	–948.4 (–943.5)	. . .	. . .	*–953.9*	*134.9*	–1083.3	–1088.8
8	–1081.0 (–1075.3)	. . .	. . .	*–1087.5*	*151.8*	–1232.8	–1239.3
9	–1215.2 (–1208.6)	. . .	. . .	*–1222.8*	*168.7*	–1383.9	–1391.5
10	–1345.8 (–1338.4)	. . .	. . .	*–1354.3*	*185.6*	–1531.4	–1539.9

[a] DFTBA; [b] BHandHLYP/3-21g(d); [c] B3LYP/6-31G(2df,p); [d] M062X/6-311+G(2d,2p); [e] QM-ESM–based $\Delta_f H_g(298\ \mathrm{K})$ using isodesmic reaction of (M, D, T)-OXMN-*n* + (2n-2) CH_3OH + (*n*-1) C_3H_8 = *n* (M, D, T)-OXMN-1 + (*n*-1) CH_3OCH_3 + (*n*-1) $(CH_3)_2CHOH$; [f] Corrected QM-ESM–based $\Delta_f H_g(298\mathrm{K})$ values using the linear regression parameters provided in the Appendix, Table A-1; [g] M062XBas3 values were derived via linear regression (f = ax + b) of DFTBA values, yielding a slope (a) of 1.00762646, an intercept (b) of 1.71696359, and a coefficient of determination (R^2) of 0.99995; [h] $\Delta H_{sub}(298\ K)$ values using the three-parameter rational function regression parameters provided in the Appendix, Table A-3.

Table 7 presents the estimated enthalpies of formation $\Delta_f H_s(298\ \mathrm{K})$ for mono-, di-, and tri-nitrate NC. The values were normalized on a per-monomer basis through division by the corresponding oligomer number. The best-fit regression equation used to extrapolate the data up to oligomer size n = 200 is also included in Table 7. The molecular weight of NC varies depending on nitrogen content and the measurement technique used. For NC with 13.3% nitrogen, viscosity measurements by Schiemann and Kühne (1934) indicated a molecular weight range of 150,000 to 220,000. In contrast, commercial collodion cotton containing 11.08% nitrogen exhibited molecular weights between 25,000 and 75,000, as determined by Medvedev (1933) using the osmotic method. Duclaux and Nodzu (1929) also employed the osmotic pressure method to analyze NC with 11.0%–12.5% nitrogen, reporting values ranging from 21,000 to 70,000. Additionally, Gralen and Svedberg (1943), using the ultracentrifuge sedimentation method, found molecular weights between 40,000 and 47,000 for NC prepared from various cellulose sources. The $\Delta_f H_s(298\ \mathrm{K})$ values converge at an oligomer size of n = 200, corresponding to molecular weights of 41,410, 50,407, and 59,404, for mono-, di-, and tri-nitrate NC, respectively (see Table 7).

Table 7. Estimates of the enthalpies-of-formation $\Delta_f H_s(298\ \mathrm{K})$ for mono-, di-, and tri-nitrate NC along with the regression equation used for extrapolation up to oligomer (n = 200).

Oligomer (n)	Mono-nitrates	Di-nitrates	Tri-nitrates
1	–223.2[a] (–223.2)[b]	–197.1 (–197.1)	–174.2 (–174.2)
2	–212.3 (–212.3)	–190.7 (–190.5)	–165.9 (–166.3)
3	–210.1 (–210.1)	–186.9 (–187.6)	–161.8 (–160.5)
4	–208.7 (–208.9)	–184.4 (–183.8)	–159.4 (–160.6)
5	–207.6 (–207.0)	–182.6 (–182.0)	–157.9 (–158.0)
6	–206.6 (–207.3)	–181.3 (–182.0)	–156.7 (–156.3)
7	–205.9 (–205.6)	–180.4 (–180.3)	–155.8 (–155.6)
8	–205.3 (–205.2)	–179.7 (–179.8)	–155.0 (–154.9)
9	–204.8 (–204.9)	–179.2 (–179.4)	–154.5 (–154.6)
10	–204.4 (–204.3)	–178.8 (–178.6)	–154.0 (–154.0)
25	–202.7	–177.7	–152.1
100	–202.6	–177.7	–152.0
200	–202.6	–177.7	–152.0
Regression equation: f = y0+a*(1–exp(–b*x))+c*(1–exp(–d*x))			
y0	–393.1517	–223.5955[c]	–194.3666
a	13.9324	45.9319	16.6422
b	0.2084	0.2728	0.2137
c	176.5833	0.3848	25.7069
d	2.9539	. . .	1.0733
R^2	0.9983	0.9972	0.9953

Note: Units in kcal/mol; The values were normalized on a per-monomer basis by dividing by the corresponding oligomer number.

[a] Values obtained from the regression equation based on the five-parameter double exponential rise to maximum model.

[b] Values in parentheses are based on $\Delta_f H_g(298\ \mathrm{K})$ at corrected M062XBas3 calculations.

[c] Values obtained from the regression equation based on the four-parameter Chapman sigmoidal model from sigma plot (regression equation: f = y0+a*(1-exp(-b*x))^c).

As with other properties, by combining the $\Delta_f H_s(298\ \mathrm{K})$ estimates for mono-, di-, and tri-nitrate from Table 7 with previously developed Monte-Carlo simulation-derived weightings (Miller and Anderson 2003), we computed enthalpies of formation $\Delta_f H_s(298\ \mathrm{K})$ as a function of various nitrogen weight percentages, as shown in Table 8 and Figure 10. Additionally, literature values for enthalpies of formation at various nitrogen contents are depicted in Figure 11 and listed in Table 9. The enthalpies of formation $\Delta_f H_s(298\ \mathrm{K})$ depend on the number of monomers per oligomer (n). We find that the value converges at an oligomer size of approximately n = 200, which falls within the experimental molecular weight range of NC. Accordingly, we report $\Delta_f H_s(298\ \mathrm{K})$ estimates of –202.6, –177.7, and –152.0 kcal/mol for mono-, di-, and tri-nitrate NC, respectively.

Table 8. Enthalpies of formation $\Delta_f H_s(298\ \mathrm{K})$ corresponding to various nitrogen weight percentages.

Nitrogen	Derived from oligomer (n)										
(%)	1	2	3	4	5	6	7	8	9	10	200
0.1	–852.6	–819.4	–807.9	–800.4	–792.5	–792.1	–785.9	–784.0	–782.5	–780.0	–774.4
0.11	–786.9	–756.7	–743.7	–737.1	–729.2	–727.8	–722.3	–720.4	–719.0	–716.5	–711.1
0.12	–721.5	–693.8	–679.2	–674.1	–666.1	–663.5	–658.9	–656.9	–655.7	–653.3	–647.7
0.126	–682.4	–655.9	–640.3	–636.4	–628.2	–625.0	–620.9	–618.9	–617.7	–615.4	–609.7
0.13	–656.4	–630.6	–614.2	–611.3	–603.0	–599.2	–595.5	–593.5	–592.4	–590.1	–584.3
0.1315	–646.6	–621.1	–604.4	–601.9	–593.6	–589.6	–586.0	–584.0	–582.9	–580.6	–574.8
0.135	–624.0	–599.0	–581.6	–580.0	–571.6	–567.2	–563.9	–561.9	–560.8	–558.7	–552.7
0.1414	–582.5	–558.2	–539.3	–539.9	–531.2	–525.8	–523.3	–521.2	–520.2	–518.2	–511.8

Note: Units in cal/g

Table 9. Literature data on standard enthalpies of formation $\Delta_f H_s(298\ \mathrm{K})$ at 298 K for NC.

Nitrogen content (%)	$\Delta_f H_s(298\ \mathrm{K})$ (cal/g)
Taylor et al. (1947)	
0.1210	–621.6
0.1265	–585.4
0.1316	–551.0
0.1324	–546.6
Jessup and Prosen (1950); Source of cellulose: cotton linters	
0.1152	–689.5
0.1218	–647.0
0.1266	–617.0
0.1346	–567.0
Jessup and Prosen (1950); Source of cellulose: wood pulp	
0.1179	–671.2
0.1218	–646.3
0.1259	–621.5
0.1343	–569.4
Purdue AAE propulsion	
0.1260	–617.0
Ioelovich (2024)	
0.0676	–978.7
0.1111	–711.9
0.1414	–525.8

Table 10 lists enthalpy-of-formation estimates for **M**-OXMN-***n***, **D**-OXMN-***n***, and **T**-OXMN-***n*** (***n*** = 1–6), obtained using various approaches. We estimated the gas-phase and condensed-phase enthalpies of formation for **M**-OXMN-***n***, **D**-OXMN-***n***, and **T**-OXMN-***n*** (***n*** = 1–6) using EDAT (Byrd 2012), a predictive tool that leverages QM-based parameters (molecular surface area, the variability of the electronic potential on the surface, etc.). EDAT, using group-equivalent methods, predicted slightly more positive values (within 6%) for $\Delta_f H_g(298\,K)$ than our estimates via quantum chemical calculations employing an isodesmic reaction scheme.

Table 10, column 4 presents the $\Delta_f H_s(298\,K)$ estimates, which were obtained by subtracting the AMBER-predicted enthalpy-of-sublimation from the M062XBas3-based $\Delta_f H_g(298\,K)$. EDAT yielded similar $\Delta_f H_s(298\,K)$ values (Table 10, column 5) for shorter oligomers ($n < 3$); however, as the oligomer length increased, the predicted values became more negative—reaching 30% lower for $n = 6$.

Table 10, column 6 presents the enthalpies of vaporization, which were estimated by a directed-message passing neural network (D-MPNN) model (Lansford et al. 2023). The values in parentheses are normalized per monomer by dividing by the corresponding oligomer number. The differences between the D-MPNN–based ΔH_v and AMBER-based ΔH_{sub} values, ranging from 7 to 10 kcal/mol, are close to the enthalpy of fusion of sugar (11 kcal/mol). This is rationalized by the fact that the ML-model was trained on vapor pressure data of liquids only (no sublimation data were included).

Table 10. Enthalpy-of-formation estimates for M-OXMN-*n*, D-OXMN-*n*, and T-OXMN-*n* (*n* = 1–6), which were obtained using various approaches.

Oligomer	$\Delta_f H_g(298\ K)$		$\Delta_f H_s(298\ K)$		ΔH_v		ΔH_{sub}	
(*n*)	QM-ESM[a]	EDAT[b]	AMBER[c]	EDAT[b]	D-MPNN[d]	EDAT[e]	AMBER[f]	EDAT[g]
				M-OMXN-***n***				
1	–193.7	–188.5	–223.2	–213.9	18.5 (18.5)	19.1 (19.1)	29.4 (29.4)	25.3 (25.3)
2	–379.8	–368.6	–424.6	–420.5	29.7 (14.9)	29.7 (14.8)	44.8 (22.4)	51.9 (26.0)
3	–568.0	–550.6	–630.4	–639.0	41.1 (13.7)	36.9 (12.3)	62.4 (20.8)	88.3 (29.4)
4	–755.2	–732.0	–835.4	–871.2	52.8 (13.2)	43.9 (11.0)	80.2 (20.0)	139.2 (34.8)
5	–937.8	–908.5	–1034.9	–1111.5	64.9 (13.0)	50.0 (10.0)	97.1 (19.4)	203.0 (40.6)
6	–1130.4	–1092.3	–1243.7	–1378.0	77.1 (12.9)	55.7 (9.30)	113.3 (18.9)	285.8 (47.6)
				D-OMXN-***n***				
1	–168.9	–164.4	–197.1	–192.4	17.3 (17.3)	20.5 (20.5)	28.2 (28.2)	28.0 (28.0)
2	–334.1	–322.4	–380.9	–384.9	27.8 (13.9)	31.7 (15.8)	46.8 (23.4)	62.5 (31.3)
3	–498.0	–476.8	–562.8	–586.1	38.8 (12.9)	40.2 (13.4)	64.9 (21.6)	109.3 (36.4)
4	–653.5	–628.3	–735.2	–806.1	50.4 (12.6)	47.6 (11.9)	81.7 (20.4)	177.8 (44.4)
5	–811.2	–783.7	–910.2	–1046.5	62.2 (12.4)	54.0 (10.8)	99.0 (19.8)	262.9 (52.6)
6	–975.5	–942.1	–1092.1	–1302.6	74.1 (12.3)	59.9 (10.0)	116.6 (19.4)	360.5 (60.1)
				T-OMXN-***n***				
1	–144.9	–142.2	–174.2	–173.4	17.9 (17.9)	21.9 (21.9)	29.3 (29.3)	31.2 (31.2)
2	–284.0	–272.2	–332.7	–346.3	28.7 (14.3)	33.2 (16.6)	48.7 (24.3)	74.1 (37.1)
3	–415.4	–396.8	–481.6	–531.4	40.8 (13.6)	40.1 (13.4)	66.2 (22.1)	134.6 (44.9)
4	–558.9	–527.4	–642.4	–738.6	53.3 (13.3)	49.1 (12.3)	83.5 (20.9)	211.2 (52.8)
5	–688.4	–649.2	–789.9	–959.7	65.8 (13.2)	56.0 (11.2)	101.5 (20.3)	310.5 (62.1)
6	–820.2	–774.0	–938.0	–1213.7	78.4 (13.1)	62.3 (10.4)	117.8 (19.6)	439.8 (73.3)

Note: Units in kcal/mol. The values in parentheses were normalized on a per-monomer basis by dividing by the corresponding oligomer number.

[a] based on M062XBas3; [b] EDAT (Byrd 2012); [c] The values were obtained by subtracting the AMBER-predicted enthalpy-of-sublimation from the M062XBas3-based $\Delta_f H_g$; [d] The enthalpy of evaporation was predicted using the D-MPNN method (Lansford et al. 2023); [e] The enthalpy of evaporation was obtained by subtracting the EDAT-predicted $\Delta_f H_l$ from the EDAT-group-approach-predicted $\Delta_f H_g$; [f] AMBER-based ΔH_{sub}; [g] The enthalpy-of-sublimation was obtained by subtracting the EDAT-group-approach-predicted $\Delta_f H_s$ from the EDAT-group-approach-predicted $\Delta_f H_g$.

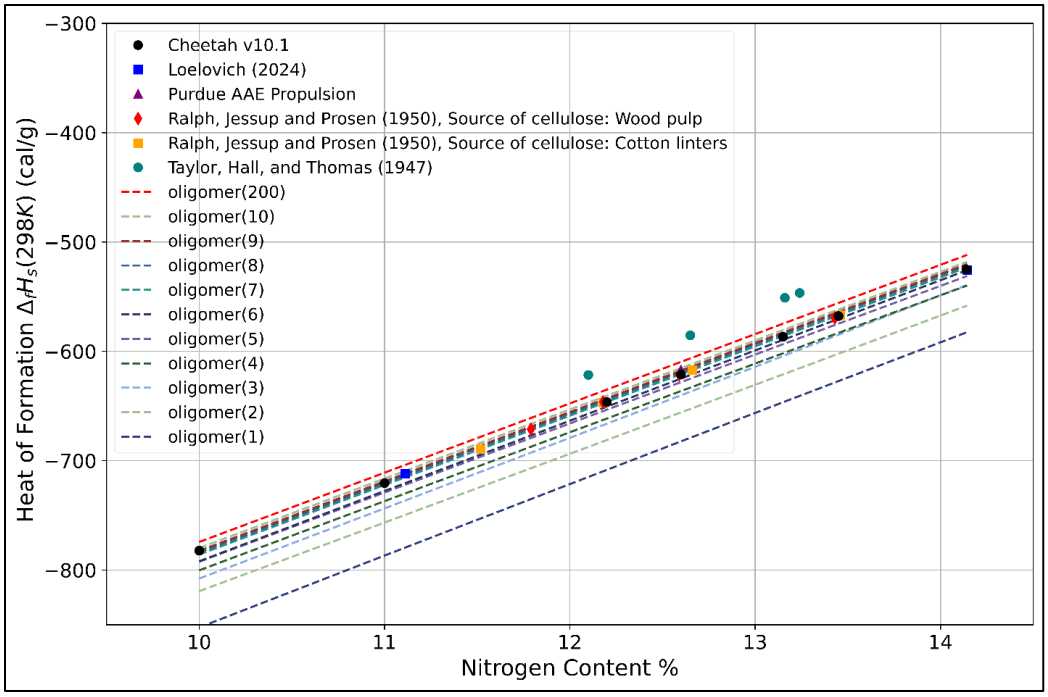

Figure 11. Enthalpy-of-formation $\Delta_f H_s(298\,\mathrm{K})$ of NC as a function of nitrogen weight percentages and compared with literature data.

4. Summary and Conclusion

This work details a computational methodology for predicting the enthalpy-of-formation of the polymer NC, a crucial property for understanding material stability and for use in combustion modeling applications. We employ a combined approach leveraging the high accuracy of ab initio methods with the efficiency of atomistic equilibrium molecular dynamics, coupled with a novel oligomeric extrapolation technique. This allows us to overcome the computational challenges associated with modeling large polymeric systems while maintaining reasonable accuracy in the calculated enthalpy-of-formation. Additionally, we leverage a Monte-Carlo sampling/weighting technique to approximate the nitrogen content of NC based on results of models of the neat mono-, di-, and tri-nitrate forms of NC oligomers (n = 1–6). This weighting methodology eliminates the need to derive overly complex and speculative MD models for the interchain structure of amorphous NC. The resulting workflow provides a robust framework for investigating the thermodynamic properties of NC (and polymers in general). It was found that model-based estimates for the pure oligomer **X**-OXMN-***n*** (X = M,D,T; n = 1–6) and the nitrogen content weighted predictions of density, cohesive energy, solubility parameter, and enthalpy-of-sublimation were quite reasonable relative to measured values. Our modeled estimates for NC with nitrogen content over the range 10.0%–14.14% fell between the measured values of Jessup and Prosen (1950)

and Taylor et al. (1947). Our estimates were closer to those of Jessup and Prosen (1950) and were also in agreement with values often used within the thermochemical code CHEETAH.

5. References

Baboul AG, Curtiss LA, Redfern PC, Raghavachari K. Gaussian-3 theory using density functional geometries and zero-point energies. J Chem Phys. 1999;110(16):7650–7657. https://doi.org/10.1063/1.478676

Barton AF. CRC handbook of solubility parameters and other cohesion parameters. Routledge; 2017.

Becke AD. Density-functional thermochemistry. III. The role of exact exchange. J Chem Phys. 1993a;98(7):5648–5652. https://doi.org/10.1063/1.464913

Becke AD. A new mixing of Hartree-Fock and local density-functional theories. J Chem Phys. 1993b;98(2):1372–1377. https://doi.org/Doi 10.1063/1.464304

Bunte SW, Sun H. Molecular modeling of energetic materials: the parameterization and validation of nitrate esters in the COMPASS force field. J Phys Chem B. 2000;104(11):2477–2489.

Byrd EFC. Simple computation of the heat of formation and density from theoretically predicted values. Army Research Laboratory (US); 2012. Report No.: ARL-TR-6206.

Chai H et al. Theoretical and experimental study on the effect of nitrogen content on the thermal characteristics of nitrocellulose under low heating rates. Cellulose. 2019;26(2):763–776. https://doi.org/10.1007/s10570-018-2100-0

Chai H, Duan Q, Cao H, Li M, Sun J. Effects of nitrogen content on pyrolysis behavior of nitrocellulose. Fuel. 2020;264:116853. https://doi.org/10.1016/j.fuel.2019.116853

Curtiss LA, Redfern PC, Raghavachari K. Gaussian-4 theory. J Chem Phys. 2007;126(8). https://doi.org/10.1063/1.2436888

Curtiss LA, Redfern PC, Raghavachari K, Rassolov V, Pople JA. Gaussian-3 theory using reduced Moller-Plesset order. J Chem Phys. 1999;110(10):4703–4709. https://doi.org/10.1063/1.478385

Duclaux J, Nodzu R. Revue générale des colloïdes. Journal de Chimie Physique. 1929;7:241–250.

French DM. The density of cellulose nitrate. J Appl Polym Sci. 1978;22(1):309–313. https://doi.org/10.1002/app.1978.070220123

Fried L, Souers P. CHEETAH: a next generation thermochemical code. Lawrence Livermore National Laboratory (US); 1994. Article Report No.: UCRL-ID-117240. https://doi.org/10.2172/95184

Frisch MJ et al. Gaussian 16 rev. C.01. Gaussian, Inc; 2016.

Gibbon CB. Large-scale atomistic simulations of cellulose and nitrated derivatives [doctoral thesis]. University of Southampton (UK); 2024. https://eprints.soton.ac.uk/486407/

Gralén N, Svedberg T. Molecular weight of native cellulose. Nature. 1943;152:625–625. https://doi.org/10.1038/152625a0

He Y et al. Experimental study on the thermal decomposition and combustion characteristics of nitrocellulose with different alcohol humectants. J Hazard Mater. 2017;340:202–212. https://doi.org/10.1016/j.jhazmat.2017.06.029

Hildebrand JH, Scott RL, editors. The solubility of nonelectrolytes. Reinhold; 1950.

Ioelovich M. Thermodynamic analysis of cellulose nitration. World J Adv Res Rev. 2024;21(3):485–494.

Jessup RS, Prosen E. Heats of combustion and formation of cellulose and nitrocellulose (cellulose nitrate). J Res Natl Bur Stand. 1950;44:387–393.

Kotter LN, Groven LJ. Hansen solubility parameters of nitrocellulose and application toward printable energetics. Langmuir. 2022;38(29):8766–8772. https://doi.org/10.1021/acs.langmuir.2c00597

Lansford JL, Jensen KF, Barnes BC. Physics-informed transfer learning for out-of-sample vapor pressure predictions. Propellants Explos Pyrotech. 2023;48(4). https://doi.org/10.1002/prep.202200265

Li Y, Lin M, Davenport JW. Ab initio studies of cellulose i: crystal structure, intermolecular forces, and interactions with water. J Phys Chem C. 2011;115(23):11533–11539. https://doi.org/10.1021/jp2006759

McQuaid MJ, Sun H, Rigby D. Development and validation of COMPASS force field parameters for molecules with aliphatic azide chains. J Comput Chem. 2004;25(1):61–71.

Medvedev AJ. Fractionation of nitrocellulose. Kunststoffe. 1933;23:249–273.

Meng W et al. Evaluation of the compatibility of energetic nitrocellulose/plasticizer blends through molecular dynamics simulation. J Ener Mater. 2024;1–18.

Miller MS, Anderson WR. CYCLOPS, a breakthrough code to predict solid-propellant burning rates. Army Research Laboratory (US); 2003. Report No.: ARL-TR-2910.

Montgomery JA, Frisch MJ, Ochterski JW, Petersson GA. A complete basis set model chemistry. VII. Use of the minimum population localization method. J Chem Phys. 2000;112(15):6532–6542. https://doi.org/10.1063/1.481224

Ochterski JW, Petersson GA, Montgomery JA. A complete basis set model chemistry .5. Extensions to six or more heavy atoms. J Chem Phys. 1996;104(7):2598–2619. https://doi.org/10.1063/1.470985

Plimpton S. Fast parallel algorithms for short-range molecular dynamics. J Comput Phys. 1995;117(1):1–19. https://doi.org/10.1006/jcph.1995.1039

Poletto M, Ornaghi HL, Zattera AJ. Native cellulose: structure, characterization and thermal properties. Materials. 2014;7(9):6105–6119. https://www.mdpi.com/1996-1944/7/9/6105

Qi X, Li H, Zhao Y, Yan N. Comparison of the structural and physical properties of nitrocellulose plasticized by N-butyl-N-(2-nitroxy-ethyl) nitramine and nitroglycerin: computational simulation and experimental studies. J Hazard Mater. 2019;362:303–310. https://doi.org/10.1016/j.jhazmat.2018.09.033

Richards LA, Nash A, Phipps MJS, de Leeuw NH. A molecular dynamics study of plasticiser migration in nitrocellulose binders. New J Chem. 2018;42(21):17420–17428. https://doi.org/10.1039/C8NJ03464H

Schiemann G, Kühne S. Cellulosechemie. 1934;15.

Sun H. Ab initio calculations and force field development for computer simulation of polysilanes. Macromolecules. 1995;28(3):701–712.

Svedberg T. The cellulose molecule. physical-chemical studies. J Phys Colloid Chem. 1947;51(1):1–18. https://doi.org/10.1021/j150451a001

Taylor J, Hall CRL, Thomas H. The thermochemistry of propellent explosives. J Phys Colloid Chem. 1947;51(2): 580–592. https://doi.org/10.1021/j150452a027

Thomas JC, Petersen EL. HTPB heat of formation: literature survey, group additive estimations, and theoretical effects. AIAA Journal. 2022;60(3):1269–1282. https://doi.org/10.2514/1.J060972

Trache D, Khimeche K, Mezroua A, Benziane M. Physicochemical properties of microcrystalline nitrocellulose from Alfa grass fibres and its thermal stability. J Therm Anal Calorim. 2016;124(3), 1485–1496. https://doi.org/10.1007/s10973-016-5293-1

Urbanski T. Chemistry and technology of explosives. Pergamon Press; 1964.

Veals JD, Chen C-C, Yeh I-C, Stone CP, McQuaid MJ. Condensed-phase property estimates for 1, 5, 9-decatriene and myrcene derived from atomistic molecular dynamics simulations. DEVCOM Army Research Laboratory (US); 2023a. Report No.: ARL-TN-1162.

Veals JD et al. Property estimates for hydroxyl-terminated polybutadiene (HTPB) type R45M derived from atomistic molecular dynamics simulations. DEVCOM Army Research Laboratory (US); 2023b. Report No.: ARL-TR-8918.

Veals JD, Lansford JL, Chen C-C, Stone CP, Cornell R. Condensed-phase property estimates for isopropyl nitrate derived from atomistic equilbrium molecular dynamics simulations. Proceedings of the 45th JANNAF Propellant and Explosives Development and Characterization Meeting; 2024 Dec 9–13; Charlotte, NC.

Yang J, Gong X, Wang G. Theoretical studies on the plasticizing effect of DIANP on NC with various esterification degrees. Computational Materials Science. 2014;95:129–135. https://doi.org/10.1016/j.commatsci.2014.07.024

Yeh I-C, Veals JD, Chen C-C, Andzelm JW, McQuaid MJ. Detailed representations for condensed phase nitrate ester reaction chemistry: part 1. Force field parameterization and validation for methyl nitrate. Proceedings of the 40th JANNAF Propellant and Explosives Development and Characterization Subcommittee Meeting; 2017 May 22–25; Kansas City, MO.

Zhao Y, Truhlar DG. The M06 suite of density functionals for main group thermochemistry, thermochemical kinetics, noncovalent interactions, excited states, and transition elements: two new functionals and systematic testing of four M06-class functionals and 12 other functionals. Theor Chem Acc. 2008;120(1–3):215–241. https://doi.org/10.1007/s00214-007-0310-x

Zheng GS et al. Parameter calibration of transition-metal elements for the spin-polarized self-consistent-charge density-functional tight-binding (DFTB) method: Sc, Ti, Fe, Co, and Ni. J Chem Theory Comput. 2007;3(4):1349–1367. https://doi.org/10.1021/ct600312f

Appendix. X-OXMN-*n* (X = M, D, T) Oligomer Gas-Phase Enthalpies-of-Formation at 298 K

This appendix lists gas-phase enthalpy-of-formation estimates at 298 K [$\Delta_f H_g(298\text{ K})$] for X-OXMN-n (X = M, D, T) oligomers. They were obtained by calculating enthalpies of reaction for (hypothetical) isodesmic reactions based on results produced by quantum mechanics-electronic structure methods (QM-ESMs). Table A-1 lists estimates of the enthalpy-of-formation $\Delta_f H_g(298\text{ K})$ and linear regression parameters for low-level models. Table A-2 lists chemical structures for target species listed in Table A-1. Table A-3 lists AMBER-based $\Delta H_{sub}(298\ K)$ and the regression equation for extrapolation up to oligomer (n) = 200. Table A-4 lists DFTBA estimates of the enthalpies of formation $\Delta_f H_s(298\text{ K})$ and the regression equation used for extrapolation up to n = 200. Figure A-1 shows AMBER-based $\Delta H_{sub}(298\ K)$ values and their best fit to the three-parameter rational model (Type I).

Table A-1. Estimates of the enthalpy-of-formation $\Delta_f H_g(298\ \mathrm{K})$ and linear regression parameters for low-level models.

ISOR[a]	High-level models									Low-level models			
	b	c	d	e	f	g	h	i	Recommended[j]	k	l	m	n
Cyclohexane + 6 C_2H_6 = 6 C_3H_8													
	–29.8	–30.1	–30.1	–29.9	–29.3	–29.1	–29.1	–29.1	–29.6	–31.3	–29.0	–29.4	–28.2
2-Methyltetrahydropyran + Cyclohexane = Cyclohexylmethane + Tetrahydropyran													
	–63.2	–63.0	–63.2	–63.1	–63.1	–63.1	–63.1	–63.1	–63.1	–63.2	–63.5	–63.3	–63.0
2-Hydroxytetrahydropyran + Cyclohexane = Tetrahydropyran + Cyclohexanol													
	–98.2	–98.0	–97.9	–97.9	–97.9	–98.0	–98.0	–98.0	–98.0	–98.9	–98.8	–98.6	–97.9
Cyclohexanol + C_3H_8 = Cyclohexane + $(CH_3)_2CH_2OH$													
	–69.6	–70.9	–70.9	–71.0	–71.0	–70.9	–71.0	–71.0	–70.8	–70.5	–71.2	–71.2	–70.9
Dihydropyran + C_3H_8 = Tetrahydropyran + C_3H_6													
	–28.7	–28.1	–28.2	–28.1	–28.1	–28.0	–28.1	–28.1	–28.2	–29.6	–29.3	–30.3	–28.4
Tetrahydropyran + C_3H_8 = Cyclohexane + CH_3OCH_3													
	–53.9	–53.5	–53.8	–53.7	–53.8	–53.7	–53.8	–53.8	–53.7	–53.6	–54.6	–54.4	–53.7
Tetrahydro-2H-pyran-2,5-diol + Cyclohexane = Cyclohexanol + 2-Hydroxytetrahydropyran													
	–135.6	–135.6	–135.6	–135.6	–135.6	–135.6	–135.6	–135.6	–135.6	–137.4	–136.1	–135.9	–135.7
Tetrahydro-2H-pyran-2,4,5-triol + Cyclohexane = Cyclohexanol+ Tetrahydro-2H-pyran-2,5-diol													
	–175.3	–175.2	–175.4	–175.3	–175.3	–175.3	–175.2	–175.3	–175.3	–175.1	–176.1	–175.9	–175.5
Tetrahydro-2H-pyran-2,3,5-triol + Cyclohexane = Cyclohexanol+ Tetrahydro-2H-pyran-2,5-diol													
	–174.7	–174.7	–174.7	–174.8	–174.7	–174.7	–174.7	–174.6	–174.7	–175.0	–174.8	-174.8	-174.7
Tetrahydro-2H-pyran-2,3,4-triol + Cyclohexane = Cyclohexanol+ Tetrahydro-2H-pyran-2,5-diol													
	–177.1	–177.1	–177.2	–177.2	–177.1	–177.1	–177.1	–177.1	–177.1	–175.7	–177.4	–177.3	–177.3
3,4-dihydro-2*H*-pyran-2,3,4-triol + Tetrahydropyran = Tetrahydro-2H-pyran-2,3,4-triol + Dihydropyran													
			–148.7	–148.7	–148.7	–148.7	–148.7	–148.7	–148.7	–150.1	–148.9	–149.1	–148.6
Xylopyranoside + Cyclohexane = Tetrahydro-2H-pyran-2,4,5-triol + Cyclohexanol													
	–215.6	–215.6	–215.8	–215.7	–215.6	–215.7	–215.6	–215.6	–215.6	–215.8	–217.0	–216.4	–216.0
M-OXMN-**1** + CH_3CH_2OH = Xylopyranoside + $CH_3CH_2ONO_2$													
			–194.2	–194.3	–194.2	–194.1	–194.2	–194.3	–194.2	–193.6	–191.2	–192.1	–193.1
D-OXMN-**1** + CH_3CH_2OH + $(CH_3)_2CHOH$ = Xylopyranoside + $CH_3CH_2ONO_2$ + $(CH_3)_2CHONO_2$													
			–169.8	–169.9	–169.8	–169.5	–169.6	–169.7	–169.7	–170.3	–164.4	–167.1	–167.2
T-OXMN-**1** + CH_3CH_2OH + 2 $(CH_3)_2CHOH$ = Xylopyranoside + $CH_3CH_2ONO_2$ + 2 $(CH_3)_2CHONO_2$													
			–147.3	–147.6	–147.5	–147.2	–147.3	–147.3	–147.4	–147.1	–139.7	–143.9	–143.2
Linear Regression[o]: f = ax+b													
a										1.00645	1.01027	1.00887	1.00203
b										1.20431	0.71389	1.01305	0.25413
R^2										0.9998	0.9983	0.9995	0.9996

Note: Units of kcal/mol.

[a] Isodesmic reactions for target species are in bold face. Reference $\Delta_f H_g(298\ \mathrm{K})$ data (in kcal/mol): C_2H_6 = –20.04; C_3H_8 = –25.02; C_3H_6 = 4.88; CH_3OCH_3 = –43.99, CH_3CH_2OH = –56.21; $(CH_3)_2CHOH$ = –65.19; $CH_3CH_2ONO_2$ = –37.92; $(CH_3)_2CHONO_2$ = –46.81; [b] APNO; [c] G4; [d] CBS-QB3; [e] G3MP2B3; [f] G3MP2//MPWB95/6-31+g(d,p); [g] G3MP2//B3LYP/6-31G(2df,p); [h] G3MP2//M062X/6-31G(2df,p); [i] G3MP2//M062X/6-311+g(2d,2p); [j] Recommended values were derived from average enthalpies of formation based on high-level models; [k] DFTBA; [l] BHandHLYP/3-21g(d); [m] B3LYP/6-31G(2df,p); [n] M062X/6-311+G(2d,2p); [o] Linear regression parameters *a* and *b* for the low-level models were fitted using recommended values.

Table A-2. Molecule structures for target species listed in Table A-1.

Cyclohexane [C_6H_{12}]	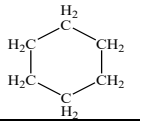
2-Methyltetrahydropyran [$C_6H_{12}O$]	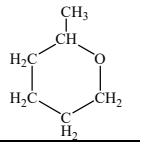
2-Hydroxytetrahydropyran [$C_5H_{10}O_2$]	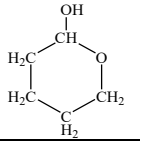
Cyclohexanol [$C_6H_{12}O$]	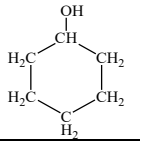
Dihydropyran [C_5H_8O]	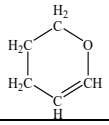
Tetrahydropyran [$C_5H_{12}O$]	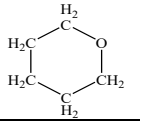
Tetrahydro-2H-pyran-2,5-diol [$C_5H_{10}O_3$]	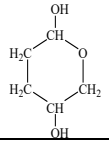
Tetrahydro-2H-pyran-2,4,5-triol [$C_5H_{10}O_4$]	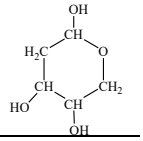
Tetrahydro-2H-pyran-2,3,5-triol [$C_5H_{10}O_4$]	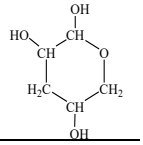
Tetrahydro-2H-pyran-2,3,4-triol [$C_5H_{10}O_4$]	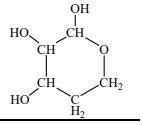
3,4-dihydro-2*H*-pyran-2,3,4-triol [$C_5H_8O_4$]	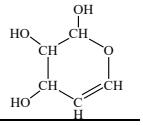
Xylopyranoside [$C_5H_{10}O5$]	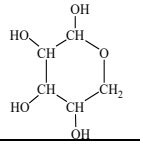

Table A-3. AMBER-based $\Delta H_{sub}(298\ K)$ and the regression equation for extrapolation up to oligomer (n) = 200.

Oligomer (n)	Mono-nitrates	Di-nitrates	Tri-nitrates
1	29.4[a] (29.4)[b]	28.2 (28.2)	29.3 (29.3)
2	22.5 (22.4)	23.4 (23.4)	24.3 (24.3)
3	20.7 (20.8)	21.5 (21.6)	22.1 (22.1)
4	19.9 (20.0)	20.5 (20.4)	20.9 (20.9)
5	19.4 (19.4)	19.8 (19.8)	20.2 (20.3)
6	19.1 (18.9)	19.4 (19.4)	19.7 (19.6)
7	18.9	19.1	19.3
8	18.7	18.8	19.0
9	18.6	18.6	18.7
10	18.5	18.5	18.6
25	17.9	17.6	17.5
100	17.7	17.2	17.0
200	17.6	17.1	16.9
Regression equation: f = (a+b*x)/(1+c*x)			
a	–12.0315	61.7262	54.2930
b	–61.7292	51.2635	33.4395
c	–3.5079	3.0059	1.9945
R^2	0.9989	0.9996	0.9996

Note: Units of kcal/mol.
[a] Values obtained from the regression equation based on the three-parameter rational model (Type I).
[b] Values in parentheses are based on AMBER calculations.

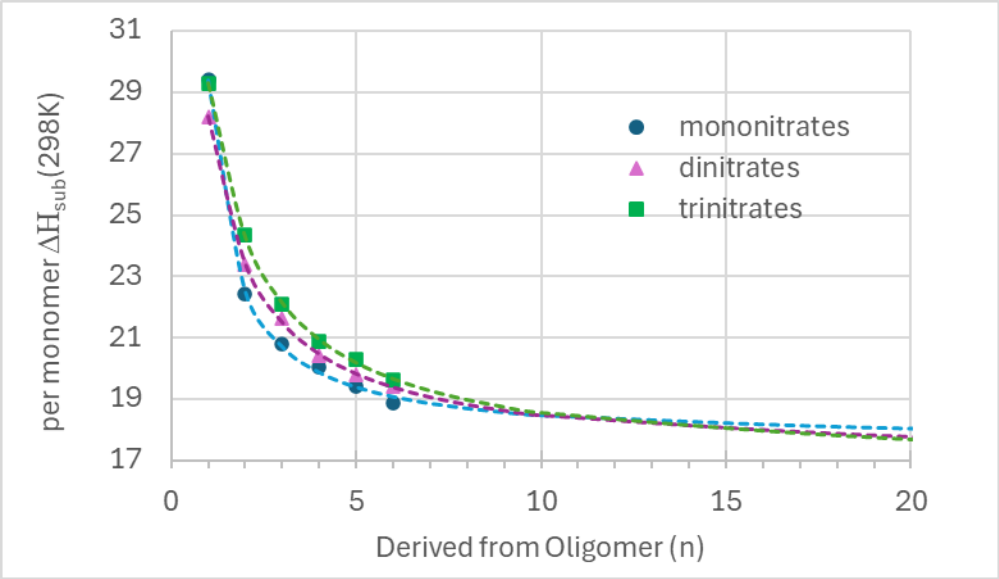

Figure A-1. AMBER-based $\Delta H_{sub}(298\ K)$ values and their best fit to the three-parameter rational model (Type I); units in kcal/mol.

Table A-4. DFTBA estimates of the enthalpies-of-formation $\Delta_f H_s(298\ \mathrm{K})$ and the regression equation used for extrapolation up to n = 200.

Oligomer (n)	Mono-nitrates	Di-nitrates	Tri-nitrates
1	–223.1[a] (–223.1)[b]	–199.0 (–199.0)	–176.8 (–176.8)
2	–211.9 (–211.8)	–189.1 (–189.0)	–165.7 (–166.0)
3	–209.7 (–209.7)	–185.2 (–185.7)	–161.2 (–160.1)
4	–208.0 (–208.3)	–183.0 (–182.7)	–158.8 (–160.0)
5	–206.6 (–206.0)	–181.6 (–181.1)	–157.2 (–157.3)
6	–205.6 (–206.1)	–180.4 (–181.0)	–155.9 (–155.6)
7	–204.7 (–204.4)	–179.5 (–179.3)	–155.0 (–154.8)
8	–204.0 (–204.0)	–178.8 (–178.8)	–154.2 (–154.1)
9	–203.5 (–203.6)	–178.2 (–178.3)	–153.6 (–153.8)
10	–203.1 (–203.1)	–177.7 (–177.5)	–153.1 (–153.1)
25	–201.5	–175.5	–151.2
100	–201.5	–175.3	–151.1
200	–201.5	–175.3	–151.1
Regression equation: f = y0+a*(1–exp(–b*x))+c*(1–exp(–d*x))			
y0	–13180.5934	–229.2673	–211.6715
a	16.5640	16.2014	18.1593
b	0.2321	0.1930	0.2209
c	12962.5793	37.7436	42.4168
d	7.3331	1.2991	1.3362
R^2	0.9986	0.9987	0.997

Note: Units of kcal/mol.

[a]Values obtained from the regression equation based on the five-parameter double exponential rise to maximum model.

[b]Values in parentheses are based on $\Delta_f H_g(298\ \mathrm{K})$ at DFTBA calculations.

List of Symbols, Abbreviations, and Acronyms

ARL	Army Research Laboratory
CED	cohesive energy density
COMPASS	condensed-phase optimized molecular potentials for atomistic simulation studies
DEVCOM	U.S. Army Combat Capabilities Development Command
DFTBA	analytic density-functional–based tight-binding method
D-MPNN	directed-message passing neural network
DoD	Department of Defense
EMD	equilibrium molecular dynamics
EODT	6-ethenyl-2,8,12,16-octadecetetraene
GAFF	general AMBER force field
HTPB	hydroxyl-terminated polybutadiene
iPN	isopropyl nitrate
MD	molecular dynamics
ML	machine learning
n	oligomer units
NC	nitrocellulose
NPT	(constant) number of particles, pressure, and temperature
PCFF	polymer consistent force field
QM	quantum mechanics
QM-ESM	quantum mechanics-electronic structure method

1 (PDF)	DEFENSE TECHNICAL INFORMATION CTR DTIC OCA
1 (PDF)	DEVCOM ARL FCDD RLB CI TECH LIB